Mon. Not. R. Astron. Soc. (2008) doi:10.1111/j.1365-2966.2008.14140.x

The low-mass initial mass function in the young cluster NGC 6611

J. M. Oliveira,⋆ R. D. Jeffries and J. Th. van Loon
Astrophysics Group, Lennard-Jones Laboratories, School of Physical & Geographical Sciences, Keele University, Staffordshire ST5 5BG

Accepted 2008 October 23. Received 2008 October 23; in original form 2008 September 23

ABSTRACT

NGC 6611 is the massive young cluster (2–3 Myr) that ionizes the Eagle Nebula. We present very deep photometric observations of the central region of NGC 6611 obtained with the *Hubble Space Telescope* and the following filters: ACS/WFC F775W and F850LP and NIC2 F110W and F160W, loosely equivalent to ground-based *IZJH* filters. This survey reaches down to $I \sim 26$ mag. We construct the initial mass function (IMF) from $\sim$1.5 $M_{\odot}$ well into the brown dwarf regime (down to $\sim$0.02 $M_{\odot}$). We have detected 30–35 brown dwarf candidates in this sample. The low-mass IMF is combined with a higher-mass IMF constructed from the ground-based catalogue from Oliveira et al. We compare the final IMF with those of well-studied star-forming regions: we find that the IMF of NGC 6611 more closely resembles that of the low-mass star-forming region in Taurus than that of the more massive Orion Nebula Cluster. We conclude that there seems to be no severe environmental effect in the IMF due to the proximity of the massive stars in NGC 6611.

Key words: stars: late-type – stars: low-mass, brown dwarfs – stars: luminosity function, mass function – stars: pre-main-sequence – open cluster and associations: individual: NGC 6611.

1 INTRODUCTION

The most favourable populations to study the low-mass initial mass function (IMF) are young, dynamically unevolved clusters, not only because they sample the entire mass spectrum but also because very low mass stars and brown dwarfs are intrinsically brighter at young ages. Properties of interest in the observed IMFs of young associations are the higher-mass slope, the mass at which the IMF reaches a maximum (turnover mass or characteristic mass) and the brown dwarf to star ratio. The local Universe high-mass IMF seems to be universal within the expected uncertainties, following a power law with approximately the Salpeter index (e.g. Massey, Johnson & DeGioia-Eastwood 1995; for a review see Elmegreen 2008). However, at the lower-mass end important differences have become apparent.

In recent years, substantial advances have been made in the study of the low-mass and substellar IMF, especially in four nearby star-forming regions: Taurus (Luhman 2004), IC 348 (Luhman et al. 2003), Chamaeleon I (Luhman 2007) and the Orion Nebula Cluster (ONC; Muench et al. 2002; Slesnick, Hillenbrand & Carpenter 2004). These populations sample different star-forming environments, from Taurus that represents the best studied example of star formation at low (stellar and gas) density to the ONC that is a relatively extreme environment (when compared to these other associations), being much denser and having a high-mass population that extends to massive O-stars. The low-mass IMF for these four regions shows important variations, namely in the turnover mass and the brown dwarf to star ratio (Luhman et al. 2006; Luhman 2007). This suggests a dependence of the IMF properties on the conditions of star formation. Star formation theories by fragmentation (Bate & Bonnell 2005; Bonnell, Larson & Zinnecker 2007), core ejection (e.g. Reipurth & Clarke 2001) and core evaporation (e.g. Whitworth & Zinnecker 2004) predict changes in the brown dwarf fraction and/or characteristic mass of the IMF depending on local environmental conditions (e.g. molecular cloud density, radiation field). Constraining any environmental dependence of the IMF might help pin down which physical parameters are important in shaping it.

The massive stars in the young cluster NGC 6611 are responsible for the ionization of the H II region M 16, the Eagle Nebula. Indeed, just the three most massive stars in the cluster central area emit nearly five times more ionizing radiation than the central Trapezium cluster of the ONC. NGC 6611 cluster members are distributed over a region of $\sim$14 arcmin radius, with a higher concentration in the largely unobscured 4 arcmin radius central area (Belikov et al. 2000). Recent distance determinations, derived using spectroscopic parallaxes (Dufton et al. 2006) and main-sequence turnoff (Bonatto, Santos & Bica 2006; Guarcello et al. 2007), favour values around 1.8 kpc. The cluster contains a large number of massive stars as well as a large population of pre-main-sequence (PMS) stars (Hillenbrand et al. 1993; Oliveira et al. 2005). The total observed mass of NGC 6611 is at least a factor of $\sim$2 larger than that of the ONC (Bonatto et al. 2006). This cluster is very young, with an age of

⋆E-mail: joana@astro.keele.ac.uk

2–3 Myr (Hillenbrand et al. 1993; Belikov et al. 2000). A considerable age spread (<1–6 Myr) has been reported for sources in the Eagle Nebula (Hillenbrand et al. 1993; Belikov et al. 2000; Dufton et al. 2006) but Indebetouw et al. (2007) find no clear evidence of age gradients throughout the region. A rich low-mass ($M \gtrsim 0.5\,M_{\odot}$) PMS population was identified by Oliveira et al. (2005) concentrated towards the most massive NGC 6611 cluster members. Many of these young stars retain dusty circumstellar discs, identified by L'-band excesses. For a comprehensive review on NGC 6611 and the Eagle Nebula, see Oliveira (2008).

In this paper, we discuss new *Hubble Space Telescope* (*HST*) observations of the central area of NGC 6611 at optical and near-IR wavelengths. These new observations are the deepest to date in this region, reaching well into the brown dwarf regime. We construct the low-mass IMF from intermediate to substellar masses by combining the *HST* data set with ground-based photometry from Oliveira et al. (2005). This manuscript is organized as follows. First, we describe the *HST* data and its reduction process and the photometry and its calibration. This is followed by the PMS identification, reddening determinations and completeness and contamination corrections, both for the *HST* data and for ground-based data. Finally, we construct the IMF for NGC 6611 and compare its main features (slope, characteristic mass and brown dwarf to star ratio) to other well-studied young clusters and associations. We discuss the implications in terms of the environmental impact on the IMF and star and brown dwarf formation scenarios.

2 OBSERVATIONS AND DATA REDUCTION

2.1 *HST* observations

The *Hubble Space Telescope* images of the core of NGC 6611 described here were obtained as part of the cycle 14 programme number 10533 (P.I. J.M. Oliveira). Optical images were obtained with the Wide Field Channel (WFC) of the Advanced Camera for Surveys (ACS; Boffi et al. 2007). A single ACS/WFC field was observed through the F775W and F850LP filters (roughly corresponding to ground-based *I* and *Z*). With a ∼0.05 arcsec pixel scale and two 2×4 K detectors, the WFC field-of-view is $\sim 3.4 \times 3.4$ arcmin^2. The system gain was set to two to completely sample the full-well-depth (as opposed to ∼75 per cent for gain 1), resulting in only a modest increase in read noise and a significant increase in the dynamic range of the observations. The total exposure time per filter is 2000 s, split into four dithered exposures of 500 s. This corresponds to one *HST* orbit per filter. The observations were designed to probe well into the brown dwarf regime, reaching down for the first time in such a distant cluster to $\sim 0.02\,M_{\odot}$.

Near-infrared images were obtained with the Near-Infrared Camera and Multi-Object Spectrometer (NICMOS; Barket et al. 2007) on board *HST*. The camera used was NIC2 with a 19.2×19.2 arcsec^2 field-of-view and 0.075 arcsec pixel. We observed 25 NIC2 fields to form a mosaic covering ∼2.5 arcmin^2. The NIC2 field positions were chosen in such a way as to avoid the bright stars in the field (Fig. 1). The filters used are F110W and F160W. These correspond loosely to ground-based *J* and *H* filters, but the reader should note that the F110W is much broader than any other commonly used *J*-band filters (0.8–1.4 μm). The total exposure time per field per filter is 128 s, split into four dithered exposures. To observe all 25 fields in both filters, five *HST* orbits were needed. The area covered by the *HST* observations in NGC 6611 is shown in Fig. 1.

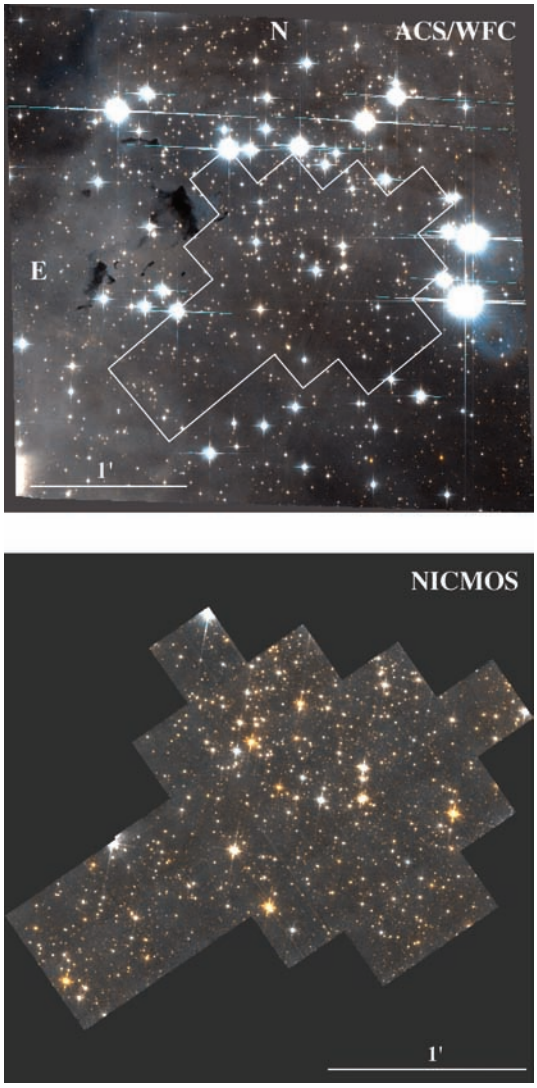

Figure 1. Top: true colour image of NGC 6611 showing the ACS/WFC field (*I* band in blue and *Z* band in red). The field centre is at $\alpha = 18{:}18{:}41.72$ & $\delta = -13{:}47{:}35.0$. The Eagle Nebula pillars are located to the south-east of this field, approximately 3 arcmin away. Bottom: true colour image showing the NICMOS mosaic (*J*-band in blue and *H*-band in red).

2.2 ACS/WFC calibrations and PSF photometry

The ACS reduction pipeline consists of two main stages: the first corrects for instrumental effects and produces calibrated data products including appropriate photometry keywords (CALACS) and the second corrects for the significant geometric distortion in WFC images, performs cosmic ray rejection and combines associated dithered data using drizzle techniques (MULTIDRIZZLE; Pavlovsky et al. 2006). For our programme, the *HST* pipeline results were a single astrometrically and photometrically calibrated image for each filter ('drz images' in units of $e^{-}s^{-1}$). The photometric zero-points are 25.256 and 24.326 mag, respectively, for *I* and *Z* (VEGAMAG magnitude system; Sirianni et al. 2005). Point spread function (PSF) photometry was performed on these pipeline images as described below.

PSF fitting packages use an optimal weighting scheme that depends on the true counts per pixel as well as readout noise and gain. To properly compute the charge transfer efficiency (CTE) correction

(see below), it is also necessary to have the total number of electrons instead of electron rate. Therefore, before applying the photometric algorithms, the drz images were multiplied by the total exposure time and the average background sky level was added back to the images (see extensive discussion by Sirianni et al. 2005).

Stellar photometry was obtained using the DAOPHOT package (Stetson 1987) within PYRAF[1] (Davis 1994), modelling the spatially variable PSF independently for each filter. Standard object detection and aperture photometry algorithms were used to detect and compute preliminary magnitudes. PSFs were constructed using a large number of stars well distributed across the images (respectively 134 and 160 stars for the *I* and *Z* bands). Stars were chosen to be bright so that the PSF in the core and wings could be well described but not brighter than ∼18.5 mag; above this limit there are clear non-linearity effects, and the PSF profiles of those stars no longer match the profiles of fainter stars. An elliptical Moffat function was chosen for the functional form of the analytical component of the PSF model and this model was allowed to vary quadratically with position in the image. Once appropriate PSF models were computed, the ALLSTAR function was used to compute photometry for all the stars in the frame; approximately 16 000 objects have measured PSF photometry in each frame. As can be seen in Fig. 1, the ACS images contain a number of bright stars that saturate the exposures and cause leakage artefacts. These artefacts cause a large number of spurious detections distributed mostly in haloes around the bright stars and on spikes along affected columns and/or rows.

The PSF photometry output files contain two output parameters that together with the magnitude error can be used to filter out spurious detections. The sharpness parameter estimates the intrinsic angular size of the object: stellar objects should have a value around zero (with a larger scatter for fainter magnitudes), while large negative and positive values identify, respectively, cosmic rays and other blemishes and resolved galaxies and blended objects. The χ^2 parameter measures the goodness-of-the-fit and should be around unity with no notable trend with magnitude. As mentioned above, bright but unsaturated stars are affected by non-linearity effects so the measured χ^2 is somewhat larger for these objects. A very good description on how imposing cuts to these parameters is used to eliminate spurious detections in catalogues can be found in Rejkuba et al. (2005). The photometric errors, sharpness and χ^2 parameters were thus used to refine each photometry catalogue, and then the *I* and *Z* detections were cross-correlated. As both filters were observed in the same visit, the positional drifts between the images are negligible, so the catalogues were matched in X and Y pixel positions before astrometry was performed: 3462 objects were detected in the combined *IZ* catalogue.

The ACS CCD detectors suffer from scattered light at long wavelengths (from about 7500 Å) and the fraction of integrated light in the scattered light halo increases as a function of wavelength. The amount of light contained in the halo will also be larger the redder the stellar source, i.e. the shape of the observed PSF depends on the colour of the star, something that PSF fitting algorithms cannot account for. The best way to mitigate this is to compute colour-dependent aperture corrections. Therefore, we were only able to calibrate in this way objects that are detected in both the *I*- and *Z*-band filters. The halo effect and the prescription on how to correct for it are described in detail in Sirianni et al. (2005), and we provide here only a summary.

A useful quantity to help estimate colour-dependent aperture corrections is the effective wavelength $\lambda_{\rm eff}$ that represents the mean wavelength of the detected photons. This source-dependent passband parameter can be used to quantify changes in the stellar light encircled in a radius *r* as a function of the stellar colour. Once $\lambda_{\rm eff}$ is determined for each source and each filter, Sirianni et al. (2005) provide a tabulated relation between $\lambda_{\rm eff}$ and aperture correction for several aperture radii.

To define a relation between $\lambda_{\rm eff}$ and observable instrumental colour, we used the function CALCPHOT in SYNPHOT (Laidler et al. 2005) and a large number of stellar template spectra. We used the following spectral atlases: the Bruzual–Persson–Gunn–Stryker atlas available within SYNPHOT (spectral types to early M) and the atlas of M-, L- and T-type dwarfs compiled by Sandy Leggett[2] with spectra from several authors (Leggett et al. 2000; Knapp et al. 2004; Chiu et al. 2006). In total, over 300 spectra were used from early-type stars to T dwarfs. With CALCPHOT, we computed instrumental $I - Z$ colours, $\lambda_{{\rm eff},I}$ and $\lambda_{{\rm eff},Z}$ to construct a linear relation equivalent to that shown in fig. 11 of Sirianni et al. (2005). For the objects in our combined *IZ* catalogue, we measured their instrumental colour, interpolated to estimate $\lambda_{{\rm eff},I}$ and $\lambda_{{\rm eff},Z}$, and interpolated Sirianni's table 6 to obtain colour-dependent aperture corrections. Computed aperture corrections are in the ranges 0.22–0.25 and 0.42–0.55 mag, respectively, for *I* and *Z*.

Another effect that needs to be corrected for is the position- and time-dependent decrease in the CCD's CTE (Riess & Mack 2004). A photometric correction can be applied that depends on the stellar flux and sky levels, on the Y position in the chip and on the time interval since the start of ACS operations. Using the prescription and coefficients described in Riess & Mack (2004), we computed magnitude corrections of up to 0.05 and 0.08 mag, respectively, for *I* and *Z*.

Once all these photometric corrections were applied, astrometry was performed using the IRAF task XY2RD. Astrometry was performed individually in the *I* and *Z* images and the positions were averaged. No absolute astrometry was performed at this stage. The final *IZ* catalogue reaches down to $I = 26$ mag and $Z = 24$ mag, with photometric errors ∼0.12 and ∼0.08 mag, respectively.

2.3 NIC2 mosaics, calibrations and aperture photometry

The NICMOS pipeline consists of two main stages: the first corrects for instrumental effects (CALNICA) and the second combines images obtained in a dither pattern and subtracts the sky background from the images (CALNICB). Due to the way in which the observations were designed, the pipeline combines the four dithered exposures for each field, but it does not combine the 25 fields in a single mosaic. Crucially, the pipeline does not correct for the geometric distortion, the largest component of that distortion being a large difference in the X and Y plate-scales. The best way to correct for these distortions and simultaneously construct complete mosaics for each of the *J* and *H* filters is to use the routine MULTIDRIZZLE in PYRAF on the output frames from the CALNICA step, i.e. on the 25×4 images per filter. This routine works in a very similar way to the second pipeline step for the ACS images. Mosaics were constructed for *J* and *H* with a final pixel scale of 0.05 arcsec, that conveniently matches the WFC pixel scale.

Before the images were mosaicked, they were corrected for the NICMOS count-rate- and wavelength-dependent non-linearity (de

[1] PYRAF is a command language for running IRAF tasks that is based on the PYTHON scripting language.

[2] http://www.jach.hawaii.edu/∼skl/LTdata.html

Jong 2006). This correction is not applied by the pipeline reduction process but a separate PYTHON routine is available.[3] The non-linearity correction amounts to 0.063 mag offset per dex change in incident flux for *J* and 0.029 mag per dex in *H*. The routine changes the count rates in the output images and therefore new zero-points are needed: 24.561 and 23.863 mag, respectively, for *J* and *H* (VEGAMAG magnitude) for images in units of $e^{-}s^{-1}$.

We initially attempted to perform PSF photometry on the *J* and *H* images as well. However, NIC2 undersamples the PSF at these wavelengths, and the PSF profile is rather complex (Krist et al. 1998); as a result we found that the quality of the PSF fits was not good, particularly for the *H* band. As our images are not crowded, we opted to use aperture photometry instead. Approximately 5000 and 10 000 sources were detected in *J* and *H*, respectively; a large number of these are spurious detections (e.g. artefacts near bright stars and at the edge of individual frames, etc.) that can be removed by combining these catalogues with the *IZ* catalogue. Aperture corrections were computed using 60–80 unsaturated bright stars. Astrometry was performed on the *J* and *H* catalogues as described above for the ACS images. Possible deficiencies in using aperture photometry are corrected for with a careful computation of completeness corrections described in Section 3.1.3.

2.4 Ground-based complementary data

To complement our *HST* catalogue at the brighter end (the *HST* images saturate for PMS objects of just over a solar mass), we used the optical and IR catalogue described in Oliveira et al. (2005), that covers a much larger area in the central region of NGC 6611. For a complete description of the observations and data reduction, the reader should refer to that article. Their catalogue includes *I* and *Z* Cousins magnitudes and *JHK* photometry in the Mauna Kea Observatory Infrared (MKO-IR) system (Tokunaga, Simons & Vacca 2002).

As noted above, the *HST* filters are very different from ground-based filter sets, and it is not trivial to convert between those systems as significant colour terms are expected (especially for cool PMS objects) due to the very different filter bandwidths. Even though there are a number of objects observed in both *HST* and ground-based filter sets, these are few and crucially they are at the bright/blue end of the *HST* data and therefore the colour range is not sufficient to derive reliable magnitude conversions. Furthermore, we have to use two different sets of PMS isochrones, as no single set covers the whole mass range we are addressing in this manuscript, from several solar masses down to the substellar regime. Therefore, we have made no attempt to merge these two photometric catalogues.

The ground-based catalogue reaches down to $\sim 0.5\,M_{\odot}$ and thus provides a good overlap in PMS stellar masses with the *HST* catalogue. As described below, we construct cluster IMFs over different mass ranges (over the same area and using methods that are similar whenever possible) and combine them for the total IMF analysis.

3 COLOUR–MAGNITUDE AND COLOUR–COLOUR DIAGRAM ANALYSIS

3.1 Low-mass stars and brown dwarfs

The *IZ*, *J* and *H HST* catalogues were combined based on their astrometry. As can be seen in Fig. 1, the *J* and *H* images cover roughly a quarter of the *I* and *Z* images. In the overlapping region, 729 objects have *IZJH* photometry – *I*-band magnitudes are the limiting ones. This is the *HST* catalogue from which PMS stars are going to be selected based on several colour–magnitude diagrams (Fig. 2).

3.1.1 Identification of PMS stars and membership selection

Fig. 2 shows the colour–magnitude diagrams used to identify the PMS population in NGC 6611. These young stars are cooler than field stars of the same apparent magnitude and thus can be easily identified in such diagrams. Selection criteria are shown in the figure, based on the observed *I* magnitude and $I-Z, I-J$ and $J-H$ colours and the position of theoretical isochrones (Baraffe et al. 1998). Using these criteria, 290 stars are identified as PMS candidates and, as such, candidate low-mass members of NGC 6611 (Table 1). A census of circumstellar discs exists for the *brighter part* of this sample ($I \lesssim 19$ mag; Oliveira et al. 2005; see also Indebetouw et al. 2007) but we do not take this information into account in order not to bias our sample selection in any way. Furthermore, no disc survey exists for the larger, fainter part of our sample.

We also show in the figure two populations of spectroscopically confirmed young very low mass stars and brown dwarfs, with ages that nicely bracket the age of the PMS population in NGC 6611 and that have been observed with the same filters:[4] Taurus (1–2 Myr; Kraus, White & Hillenbrand 2006) and Upper Scorpius (∼5 Myr; Kraus, White & Hillenbrand 2005). The position of these objects in the diagram shows that our selection region is generous enough to include a PMS population of age <5 Myr; our selection therefore should not exclude any PMS objects.

The foreground loci in the colour–magnitude diagrams are sparsely populated so contamination by foreground dwarfs is not large; this was expected since the area we are analysing is relatively small. The cuts shown in the figure, in particular the cut in $J-H$ colour, are also very effective in separating the PMS population from the large number of heavily reddened stars towards the Galactic centre. These stars delineate a well-defined sequence with $I-Z$, $I-J$ and $J-H$ colours in the narrow ranges 2–3, 4.5–6 and 2–2.5 mag, respectively. Our *HST* survey is so deep that in order to understand the nature of this heavily reddened population, we need to consider what lies behind the cluster towards the Galactic centre.

The line-of-sight towards the Eagle Nebula encounters the Scutum-Crux spiral arm at a distance of <4 kpc (Vallée 2008). Recent three-dimensional Galactic interstellar extinction maps (based on Two Micron All Sky Survey (2MASS) data; Marshall et al. 2006) show that behind NGC 6611 there is a marked extinction jump consistent with the location of this spiral arm: between 2.8 and 3.5 kpc from the Sun, extinction as measured by A_K increases from ∼0.6 to ∼1.4 mag. This suggests that the distinct clump of reddened stars could be part of the Scutum-Crux spiral arm structure. To test this hypothesis, we use evolutionary tracks from Marigo et al. (2008) for a 5-Gyr-old population and solar metallicity, computed for the *HST* ACS and NICMOS filter sets. Two such tracks are shown in Fig. 2: the bluest for a distance of 2500 kpc and $A_V = 13$ mag, and the reddest for 3500 kpc and $A_V = 17$ mag. These tracks encompass the observed population very well. Therefore, even though the distance and extinction estimates are very approximate, the population with

[3] http://www.stsci.edu/hst/nicmos/performance/anomalies/nonlinearity.html

[4] These objects were observed with the same filters but with the *HST* ACS/HRC camera; very small colour-dependent transformations are applied to convert the ACS/HRC measurements to magnitudes as would be observed with the ACS/WFC camera.

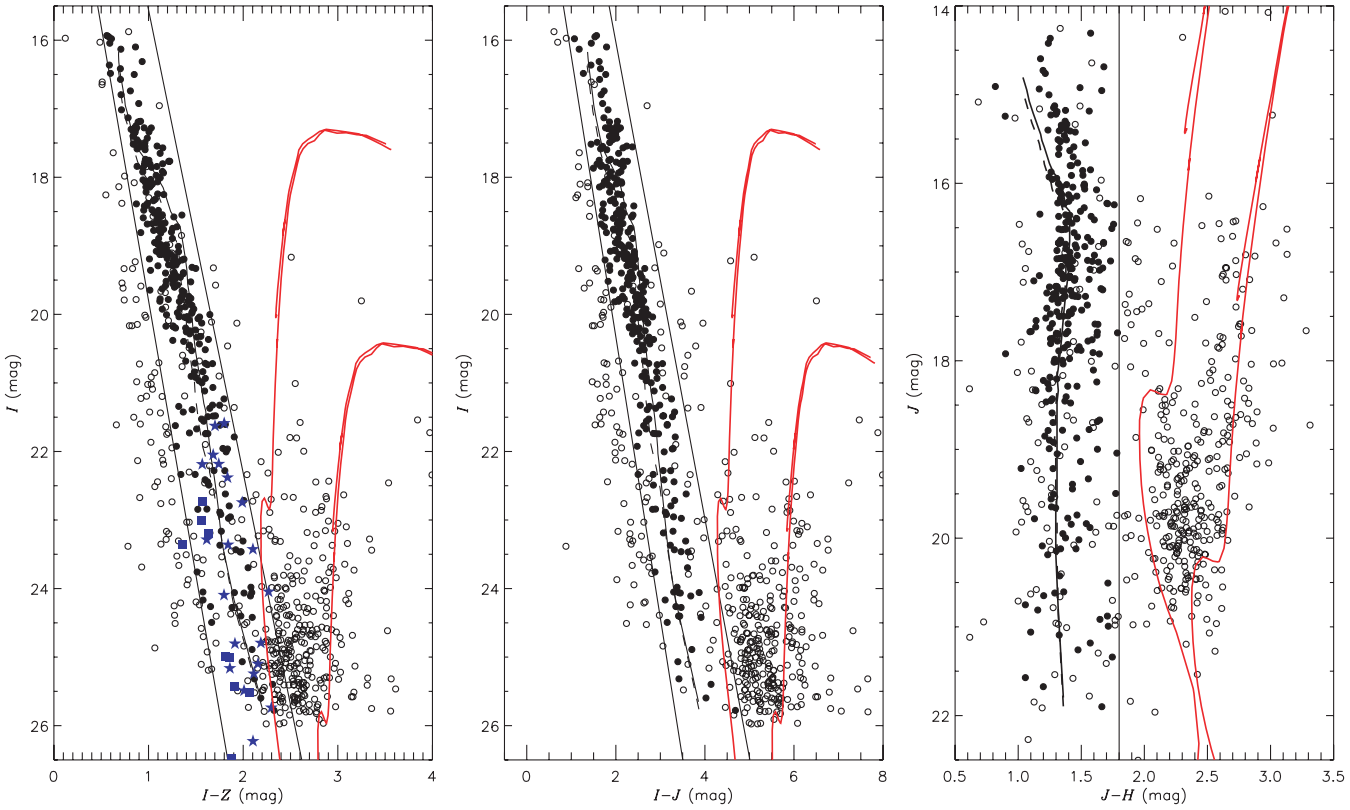

Figure 2. Colour–magnitude diagrams of the *HST* survey area. The straight lines indicate the regions for selection of PMS candidates: open circles are all objects with *IZJH* photometry while filled circles mark the PMS candidates. Note the large number of heavily obscured stars towards the Galactic centre with $J - H \sim 2$– 3 mag. PMS isochrones for 2 Myr (full line) and 3 Myr (dashed line) from Baraffe et al. (1998), assuming average extinction (Section 3.1.2) and a distance of 1.8 kpc, are also shown. Red lines are isochrones from Marigo et al. (2008) for distance and extinction consistent with an evolved population in the Scutum-Crux spiral arm (see text). Blue squares and stars are Upper Scorpius (Kraus et al. 2005) and Taurus (Kraus et al. 2006) very low mass and brown dwarf cluster members, of ages, respectively, ∼5 and 1–2 Myr, observed with the same filters and placed at the same distance and average extinction as NGC 6611.

Table 1. NGC 6611 cluster candidates selected from the *HST* photometric catalogue. Absolute astrometry was performed on this catalogue using the positions of ∼40 bright stars that are also detected in the catalogue of Oliveira et al. (2005), that was astrometrically calibrated against *2MASS*. The precision in the positions is better than 0.04 arcsec in each coordinate. Columns provide the magnitudes and errors for I, Z, J and H. $E(B-V)_{2\,\mathrm{Myr}}$ and $E(B-V)_{3\,\mathrm{Myr}}$ are the extinction determinations using the 2 or 3 Myr isochrones. Based on these determinations, candidates are classified as members [$0.45 < E(B-V) < 1.0$ mag] or non-members (see Section 3.1.2). $M_{2\,\mathrm{Myr}}$ and $M_{3\,\mathrm{Myr}}$ are the masses of PMS objects, assuming an age of either 2 or 3 Myr. (Please see the Supporting Information section for details of the full table.)

RA ($^{\mathrm{h}}$ $^{\mathrm{m}}$ $^{\mathrm{s}}$)	Dec. ($^{\circ}$ $'$ $''$)	I (mag)	Z (mag)	J (mag)	H (mag)	$E(B-V)_{2\,\mathrm{Myr}}$ (mag)	$E(B-V)_{3\,\mathrm{Myr}}$ (mag)	Status	$M_{2\,\mathrm{Myr}}$ ($\mathrm{M}_{\odot}$)	$M_{3\,\mathrm{Myr}}$ ($\mathrm{M}_{\odot}$)
18:18:46.09	−13:43:01.3	17.842 ± 0.021	16.754 ± 0.011	15.674 ± 0.002	14.354 ± 0.002	0.54 ± 0.08	0.55 ± 0.06	Member	0.678	0.750
18:18:46.06	−13:43:02.3	19.032 ± 0.012	17.893 ± 0.015	16.846 ± 0.004	15.500 ± 0.003	0.58 ± 0.06	0.58 ± 0.05	Member	0.402	0.457
18:18:46.02	−13:43:05.8	20.934 ± 0.014	19.334 ± 0.014	18.009 ± 0.008	16.708 ± 0.006	0.63 ± 0.05	0.64 ± 0.05	Member	0.132	0.164
18:18:45.75	−13:42:47.1	20.032 ± 0.026	18.622 ± 0.015	17.468 ± 0.005	16.047 ± 0.004	0.71 ± 0.05	0.78 ± 0.05	Member	0.270	0.334
18:18:45.71	−13:42:44.1	19.473 ± 0.019	18.192 ± 0.017	17.099 ± 0.004	15.975 ± 0.004	0.31 ± 0.05	0.34 ± 0.05	Non-member		
18:18:45.71	−13:42:47.2	19.717 ± 0.019	18.354 ± 0.016	17.223 ± 0.004	15.861 ± 0.004	0.62 ± 0.05	0.68 ± 0.05	Member	0.284	0.350
...										

redder colours is entirely consistent with what we would expect for a population in that spiral arm, at a range of distances and extinctions consistent with the 2MASS extinction profile. This population, that would include both main-sequence and evolved stars, seems to be an important source of contamination. However, Fig. 2 shows that these stars are so much redder than genuine cluster members that they are effectively excluded by the $J - H$ cut we apply for PMS selection. Other sources of contamination are discussed further in Section 3.1.4.

3.1.2 Cluster reddening and de-reddening of PMS stars

The first step to analyse a PMS population in a region like NGC 6611 is to determine intrinsic magnitudes, i.e. to correct for reddening. Many authors have studied the extinction properties towards the Eagle Nebula (e.g. Hillenbrand et al. 1993; Belikov et al. 1999, 2000; Dufton et al. 2006); the optical extinction (A_{V}) is variable and the values of R_{V} (the ratio of total to selective extinction), estimated on a star-by-star basis, are larger than the normal interstellar medium

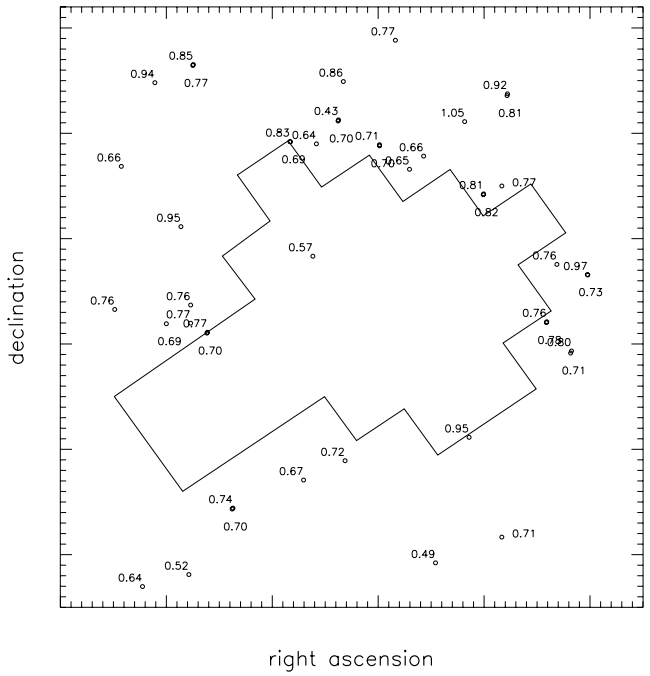

Figure 3. Schematic diagram showing our survey area and published measurements of $E(B-V)$ towards O and B stars in NGC 6611, from Dufton et al. (2006), Belikov et al. (1999) and Belikov et al. (2000). The typical value for the survey area is $E(B-V) \sim 0.70$ mag, with measurements in the range 0.45 to 1 mag.

(ISM) value. Reported R_V values are in the range 3.5–4.8 (typical value ∼3.75, Hillenbrand et al. 1993) while $E(B-V)$ values vary between 0.5 and 1.1 mag. Towards the NGC 6611 cluster extinction is, however, at the lower end of this range (Belikov et al. 1999; Indebetouw et al. 2007).

The way in which we designed the NICMOS observations (i.e. avoiding the bright stars) means that we do not have independent extinction determinations towards the survey area. However, as can be seen from Fig. 3, that area is surrounded by many stars with reddening measurements. Thus a typical $E(B-V)$ towards the survey area is of the order of 0.70 mag with an observed spread of ∼0.45–1.0 mag, corresponding to $A_V \sim 2.6$ mag and a range of ∼1.7–3.75 mag – we adopt $R_V = 3.75$ for cluster members. Thus, extinction is relatively low in the central cluster area but it is also variable even at small spatial scales.

Accordingly, we have opted to compute extinction towards individual PMS candidates using the two colour–colour diagrams shown in Fig. 4. Also shown are the Baraffe et al. (1998) PMS isochrones (these authors have produced absolute magnitudes for the four *HST* filters used in this analysis.). Using the stellar spectral atlases and procedure described previously, we compute *HST* colours for a large number of dwarfs in order to construct a dwarf locus down to spectral type M8–M9. Reddening vectors are computed using the same template spectra and the reddening curve of Cardelli, Clayton & Mathis (1989) adopting $R_V = 3.75$: the spectra are reddened with a range of $E(B-V)$ values, and SYNPHOT is used to estimate the extincted colours through the *HST* filters. The resulting reddening slopes are $A(I) = 2.435 \times E(B-V), A(Z) = 1.86 \times E(B-V)$, $A(J) = 1.30 \times E(B-V)$ and $A(H) = 0.76 \times E(B-V)$.

PMS stars have lower surface gravities than main-sequence dwarf stars, and thus populate colour–colour diagrams in the region between dwarfs and giants (see also Oliveira, Jeffries & van Loon 2004). As can be seen from Fig. 4, there are sizable differences between the isochrones and the determined dwarf loci. We did not have many late-M dwarf spectra available to constrain the reddest loci colours, and we do not see evidence in our data set of the sharp turn to redder $J-H$ colours that seems to occur for these spectral types: the variation of the $J-H$ colour for M dwarfs is ∼0.4 mag, while for our PMS candidates the observed $J-H$ spread is ∼0.3 mag, even with possible variable extinction effects. We have therefore decided to de-redden the PMS candidates using the set of PMS isochrones that are being used for the mass determination (Baraffe et al. 1998).

Fig. 4 shows that the Baraffe isochrones in the colour–colour diagrams are somewhat age-dependent. The dependence is small and only affects stars in a small range of observed colours. Nevertheless, we adopt two values for the age of NGC 6611, 2 and 3 Myr, consistent with the higher-mass population (Hillenbrand et al. 1993; Belikov et al. 2000). We will keep these calculations completely independent, i.e. we obtain independent IMFs for these two assumed ages in order to isolate the effect of fixing the age of the population.

Using the reddening vector and the isochrones, $E(B-V)$ is computed for each star in each diagram; when available the two

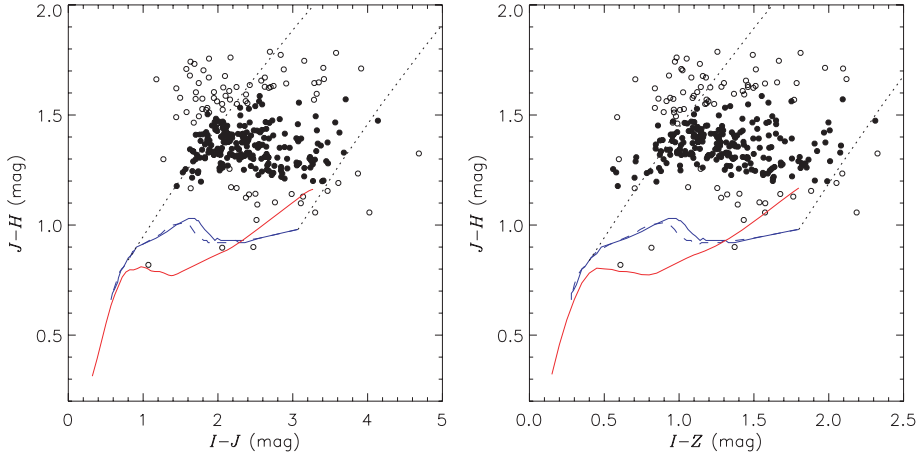

Figure 4. Colour–colour diagrams for the PMS candidates selected from the *HST* photometric catalogue. The full and dashed blue lines are Baraffe et al. (1998) isochrones, respectively, for 2 and 3 Myr. The dotted lines represented the reddening band derived for the *HST* filters. Dwarfs from archival spectral atlases (see text) were used to empirically derive the dwarf loci (red lines, to spectral type M8–M9). Filled circles are the PMS objects with final reddening determination between 0.45 and 1.0 mag (see Fig. 5).

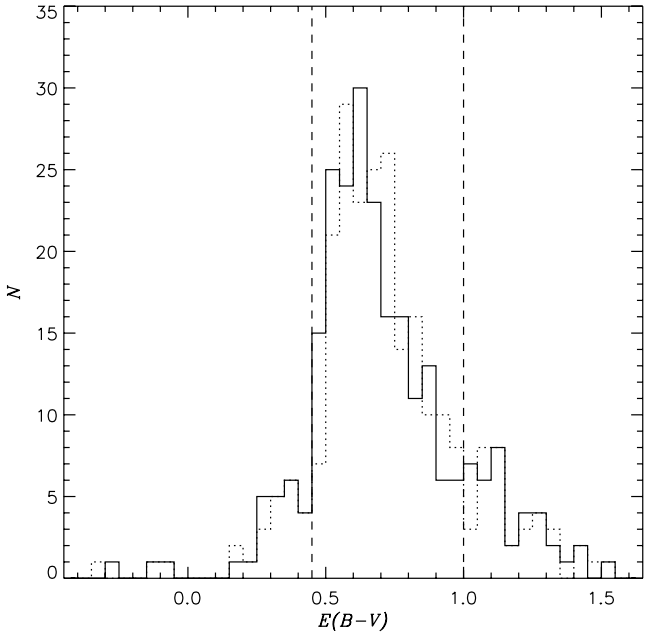

Figure 5. Histograms of the $E(B-V)$ determinations, using the 2 Myr (full line) and 3 Myr (dotted line) isochrones. These determinations are consistent with the average $E(B-V)$ towards massive cluster members [$E(B-V) = 0.7$ mag]. Vertical dashed lines show the cuts used to refine membership (see text).

estimated $E(B-V)$ values are averaged. Error bars are computed for these estimates, including contributions from photometric errors in the observed colours and the uncertainty introduced by the choice of the reddening vector – the reddening vector slope changes somewhat depending on the spectral energy distribution of the star, see previous discussion on $\lambda_{\rm eff}$.

A feature in these diagrams is the 32 stars that cannot be de-reddened because they do not have a reddening vector intersection with the isochrones. Three of these objects are too red for the available theoretical colours. The remaining 29 objects have observed $J-H$ colours that seem too red for their observed $I-J$ and $I-Z$ colours and thus cannot be de-reddened on to the PMS loci. Closer inspection of Fig. 4 suggests that the majority of those stars would be too reddened to be considered bona fide cluster members. These stars are relatively bright thus *if they were NGC 6611 members* they should have an intrinsic PMS $(J-H)_0 \lesssim 0.9$ mag. If we de-redden these objects using only their $J-H$ colour to a conservative intrinsic colour of $(J-H)_0 = 0.9$ mag, the estimated $E(B-V)$ for most objects would be in the range 1.0–1.7 mag with only three objects having $E(B-V) < 1.0$ mag. Therefore, of these 29 objects all but three would be rejected for having reddening too large when compared to the reddening distribution of more reliable cluster members (see Fig. 5 and discussion on reddening cuts below). It is likely that these objects are actually behind the cluster and not PMS objects.

Some earlier type stars fall in the region of the diagrams where the de-reddening procedure has two solutions. For these stars we computed two extinction solutions, i.e. one to the 'late-type branch' (with $0.9 < J-H < 1.0$ mag) and one to the 'early-type branch' (with $0.6 < J-H < 0.9$ mag). We find that the $E(B-V)$ values determined to the 'late-type branch' are consistent with the $E(B-V)$ cluster distribution (Fig. 5). We note that the extinction determinations for these objects have larger error bars reflecting the uncertainties of the procedure.

Fig. 5 shows the histograms of $E(B-V)$ values determined towards PMS candidates. The mean of the distribution is consistent with the average $E(B-V)$ measured towards massive cluster members (Fig. 3). Its standard deviation is of the order of 0.15 mag; when compared to the typical $E(B-V)$ error of 0.07 mag, this again suggests that local variations of extinction are real, as can be seen from the images themselves and Fig. 3. The range of $E(B-V)$ values in Fig. 5 [$0 < E(B-V) < 1.5$ mag] is larger than the range measured towards massive cluster members [$0.45 < E(B-V) < 1.0$ mag], suggesting that the PMS candidate sample includes some foreground and background contaminants. We use these histograms to refine cluster membership: objects that have $E(B-V)$ values in the range 0.45–1.0 mag (the same as the massive cluster members) are kept in the PMS sample. Our survey is so deep that reddened stars behind the cluster can contaminate the PMS selection (Section 3.1.1). The upper reddening cut is essential to exclude as many of those objects as possible (see Section 3.1.4); the lower cut eliminates some foreground dwarfs. We note that, so long as reddening is not mass dependent and the intrinsic loci and reddening vectors are not in error in a mass-dependent way, then reddening cuts should not affect the derived shape of the IMF, even if they were too stringent.

Oliveira et al. (2005) determined that approximately 55 per cent of the objects brighter than $I = 19$ mag show an excess in the L'-band indicative of the presence of a circumstellar disc, while only ∼18 per cent of those objects show such an excess in the K band. *IZJH* magnitudes are generally much less sensitive to disc excesses (e.g. Oliveira et al. 2005; Robitaille et al. 2007) and therefore this should not significantly affect our reddening determinations. Nevertheless, our reddening cuts (see above) are generous enough to accommodate uncertainties in the reddening determination.

The final PMS sample includes 208 objects. Once extinction is computed, intrinsic I-band magnitudes are calculated, taking care to propagate the errors introduced by the extinction calculation. Then assuming either an age of 2 or 3 Myr and adopting a distance of 1.8 kpc, masses are computed for each object using their intrinsic I-band magnitudes and the Baraffe et al. (1998) isochrones. For this sample, estimated masses range from 0.02 to 1.5 $M_\odot$ (Table 1). In the next sections, we deal with two crucial issues in IMF analysis: completeness and contamination.

3.1.3 Completeness correction

Many bright stars are saturated in the *HST* images and create image artefacts that can prevent the detection of fainter stars nearby. We also need to characterize the reduced detection sensitivity at the fainter end. In order to address the issue of completeness of the photometric catalogues we construct fake star simulations: replicas of PMS stars (i.e. stars with true PMS magnitudes in I, Z, J and H), randomly selected from the observed I-band luminosity function (LF), are introduced into four *HST* images, at random positions. For simplicity in generating the randomized star positions, this experiment was performed in the central 1.2 arcmin^2 area of the survey. One hundred sets of fake stars were created, each with 100 randomly selected PMS replicas. In each simulation, the number of objects in the central region was increased by about 1/4, thus not changing the crowding properties of the field in any significant way.

In order to introduce the replica PMS stars in the images, we use the PSFs determined for each filter and the ADDSTAR procedure in IRAF. As described in Section 2.3, for the J and H band we computed PSFs for the mosaics but ultimately opted to use aperture photometry in the final catalogue. We tested the procedure of

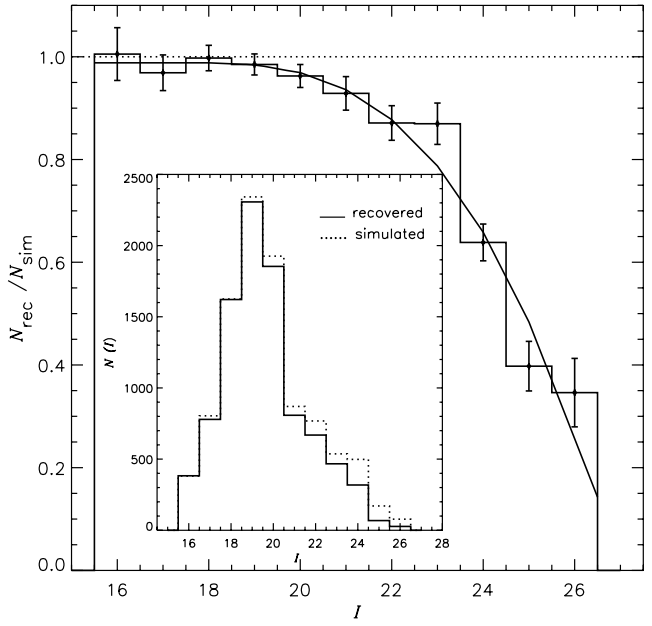

Figure 6. Completeness correction versus *I*-band magnitude. The histogram (with Poissonian error bars) shows the recovery rate as a function of magnitude (see text). The full line is a second-degree polynomial used to represent the completeness correction as a function of *I*-band magnitude. The inset shows the histograms of simulated and recovered *I*-band magnitudes.

adding stars to the mosaics using the computed PSFs and then performing aperture photometry on those stars and it works well: stars are recovered at a similar rate as for the *I* and *Z* images and their magnitudes are preserved.

The complete data reduction procedure, exactly as described in the previous sections, was repeated for each of the 100 simulations, including (PSF or aperture) photometry, aperture and linearity corrections, astrometry, catalogue matching, etc. and PMS selection. Finally, the input and recovered *I*-band LFs are compared: of the 10 000 stars simulated 9301 were recovered. The recovered stars are not only detected in *I*, *Z*, *J* and *H* but they also have colours consistent with PMS selection, i.e. of the PMS stars simulated approximately 93 per cent are recovered *and selected as PMS objects*. This is what we mean by 'recovery rate'.

Fig. 6 shows the recovery rate as a function of *I*-band magnitude, as well as the histograms for the simulated and recovered *I*-band magnitudes. There is a slight magnitude creep, i.e. more stars are recovered in some of the brighter magnitude bins than were originally simulated (Naylor et al. 2002), due either to statistical uncertainty or to the presence of another star nearby (see also Stetson 1991). As at the brighter end no stars are lost, this can result in a recovery rate larger than 1 for some bins. At the fainter end, the recovery rate is as low as 35 per cent. We should point out that in the combined *IZJH* catalogue completeness effects are mostly introduced by the *I* and *Z* catalogues: the *J*- and *H*-band images are deeper and are less affected by saturation artefacts. To construct the completeness function, we fitted a second-degree polynomial to the recovery rate for $I < 18$ mag; for brighter magnitudes, the recovery is constant at $\sim$1. For each object in the PMS sample a weight is assigned equal to the inverse of the completeness correction at its observed *I*-band magnitude; these weights are used to compute completeness-corrected IMFs.

3.1.4 Field star contamination

To make a quantitative estimate of the effect of contamination in our catalogues, we follow the procedure first outlined by Jeffries et al. (2004). First, a field star population is simulated using an *I*-band LF for dwarfs in the Galactic disc. We adopt the disc M dwarf *I*-band LF $\Phi(M_I)$ of Zheng et al. (2004), complemented at the brighter end with $\Phi(M_V)$ compiled by Reid & Hawley (2000), where $\Phi(M_V)$ is converted to $\Phi(M_I)$ using average $V - I$ dwarf colours (Leggett 1992; Leggett et al. 1996). Using this LF (in units of stars pc^{-3} mag^{-1}) as a weighting function, absolute *I* magnitudes and intrinsic colours were randomly assigned to a very large number of simulated stars. The spatial density of stars is described by N_0 $\exp(-(R - \mathrm{R}_\odot)/h_R)$ $\exp(-Z/h_Z)$, where $Z = |\mathrm{Z}_\odot + d \sin(b)|$ is the height above the Galactic plane, $\mathrm{Z}_\odot = +27$ pc is the height of the Sun above the plane, d is the heliocentric distance, b is the Galactic latitude, $h_Z = 270$ pc is the scaleheight, R is galactocentric distance, $h_R = 2250$ pc is the scalelength and N_0 is the space density in the plane ($Z = 0$) at the solar galactocentric distance of $\mathrm{R}_\odot = 8600$ pc (Chen et al. 2001).

The intrinsic *I*-band magnitudes of stars with spectral types from A0 to M9 were compiled from several sources in the literature (Bessell & Brett 1988; Gray 1992; Leggett 1992; Leggett et al. 1996) while average colours were derived for the *HST* filters in Section 3.1.2. We then populated a cone of length 7200 pc in the direction of NGC 6611 according to the density behaviour described above, selecting stars randomly from the list previously generated. The opening angle of the cone simulates an area 10 times larger than our real survey area to ensure that the contamination correction plays no role in the statistical uncertainties of the IMF.

The next step is to describe the extinction profile towards and *behind* NGC 6611. Belikov et al. (1999) show that the reddening distribution of field stars towards the cluster has two peaks, one identified as a low-extinction foreground population and a second as a reddened background population obscured by the molecular cloud. The $E(B - V)$ values measured towards both the massive cluster members and PMS stars seem to show a real spread in extinction. This suggests a first extinction screen associated with the cluster's parent molecular cloud. The analysis in Section 3.1.1 strongly suggests that there is a second extinction screen behind the cluster, probably associated with another spiral arm structure.

We take all this information into account to construct a prescription for the behaviour of extinction as a function of distance along the line-of-sight towards NGC 6611. We assumed that $E(B - V)$ has a double-step-like behaviour: it grows linearly with distance at the rate of 0.25 mag kpc^{-1}, reaching $A_\mathrm{V} = 1.7$ mag at the cluster position and then immediately increasing to $A_\mathrm{V} = 3.7$ mag (in agreement with measurements towards cluster members). Behind the cluster, extinction continues to increase at 0.25 mag kpc^{-1} until the position of the second extinction screen. At a distance of 2500 pc, extinction climbs to $A_\mathrm{V} \sim 13$ mag, consistent with the 2MASS extinction profile from Marshall et al. (2006). After that, extinction increases linearly to a maximum simulated distance of 7200 pc. We adopt $R_\mathrm{V} = 3.75$ mag up to and including the cluster position (the extinction behaviour is dominated by the average dust properties *in the molecular cloud*), while behind the cluster we adopt $R_\mathrm{V} = 3.1$, more consistent with the average properties of the Galactic ISM. Each star in the simulation has extinction applied to its magnitudes according to its simulated distance and following this two-step function. Finally, the simulated apparent magnitudes are perturbed according to the observed distribution of measurement errors in the photometric catalogue.

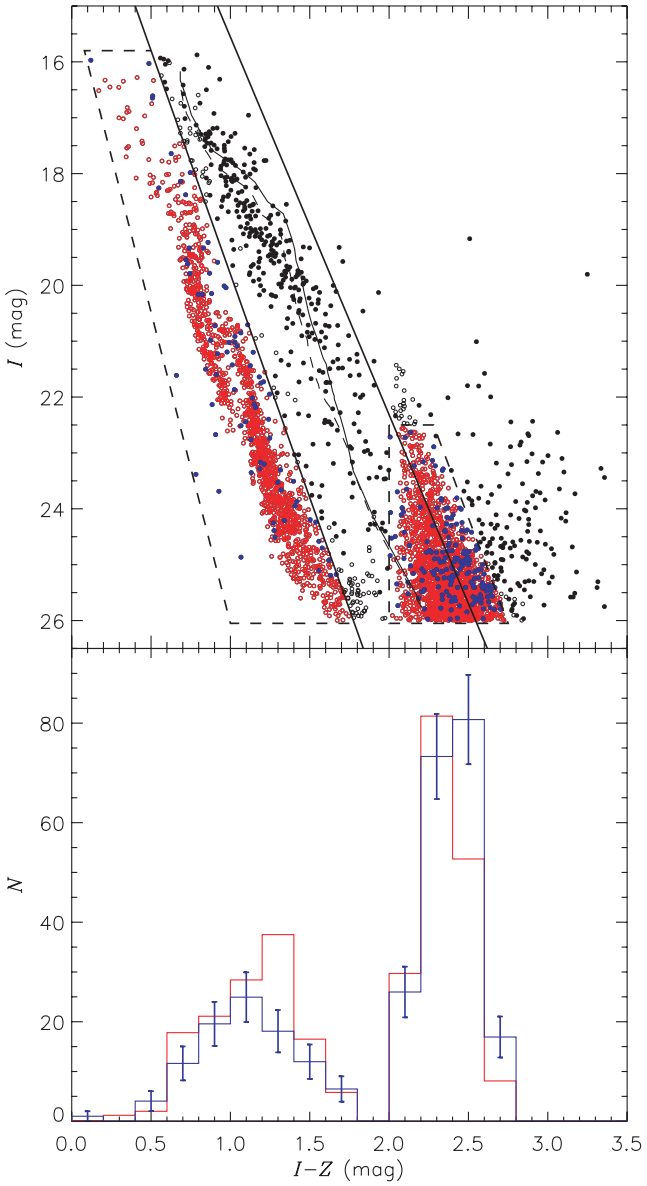

Figure 7. Colour–magnitude diagram of the simulated and observed catalogues (open and filled circles, respectively). Coloured symbols are the objects used for the comparison between the observed and simulated catalogues (respectively blue and red symbols). The bottom panel shows the $I - Z$ colour histograms for two areas in the colour–magnitude diagram (dashed boxes): below the PMS selection region and at the location of the reddened star population. The simulated area is 10 times larger than the *HST* field; the histogram has been renormalized to equal area. In terms of the number of objects in each colour bin, the simulated (red histogram) and observed (blue histogram) catalogues agree very well. The simulation does not, however, produce objects redder than about $I - Z \sim 2.8$ mag (see text). Simulated objects that fall into the PMS selection region are potential contaminants, but are largely excluded on the basis of their reddening (see text).

Fig. 7 shows a colour–magnitude diagram: filled and open circles represent the observed and simulated catalogues, respectively. The simulated catalogue seems to successfully reproduce the observed colour–colour and colour–magnitude diagrams in terms of the different stellar populations present: the foreground population, the moderate extinction background population and the heavily reddened population at larger distance behind the cluster. To test whether the simulated catalogue also quantitatively produces the correct numbers of stars we investigated in more detail two particular regions in the *IZ* diagram: just below the PMS selection area and the region where the clump of stars with redder colours are observed. The comparison of the numbers of simulated and observed stars in colour bins is also shown in Fig. 7. For these two representative regions, the simulated catalogue produces stellar numbers that are entirely consistent with the observed catalogue.

However, the simulated catalogue does not produce stars with more extreme red colours ($I - Z > 2.8$ mag). There are several possible reasons for this. The properties of the very reddened population are sensitive to the details of the extinction profile in the simulation, such as the location and magnitude of the second extinction jump, the fact that we do not account for any structure or clumpiness in the ISM and the adopted reddening coefficients. At large extinctions, these coefficients are manifestly not constant and they also depend on the intrinsic colours of each object. Furthermore, we only simulate main-sequence objects; this reddened population has evolved stars associated with it, brighter and redder objects that we simply do not simulate. The properties of the first extinction jump affect only the population underneath the PMS selection region. Another source of uncertainty is the parameters associated with the Galactic stellar density distribution, particularly h_R (Chen et al. 2001).

In spite of all these caveats, our simulation is able to reproduce the observed catalogue quite well. Fig. 7 shows that the number of possible contaminants (i.e. simulated objects that fall into the PMS selection region) is very small, even for such a deep survey. The heavily extincted background population is effectively removed by the $J - H$ colour cut for PMS selection (Fig. 2). By using reddening cuts (see Section 3.1.2), we are further able to exclude the majority of possible contaminants from the foreground and moderately extincted background populations. The application of the reddening cuts also means that the exact details of the extinction behind the cluster are not crucial; as the area considered here is small, the number of foreground contaminants is so small that foreground extinction is also not an issue. However, some objects from the former population can have similar extinction as the young cluster, and thus contaminate the PMS selection region. These contaminants need to be taken into account when constructing the mass function (MF).

The procedure described here to mimic field star contamination produces a catalogue that is processed in exactly the same way as the observed stellar catalogue. A PMS and reddening selection are performed on the simulated catalogue: there are only 52 simulated contaminants in the PMS selection region, and of these only 17 or 14 fulfil the reddening requirements (respectively using the 2 or 3 Myr isochrones). For these objects, intrinsic *I*-band magnitudes and stellar masses are estimated. The derived masses are used to compute a contamination MF. This MF is divided by 10 because the simulated area is 10 times larger than our actual survey. We find that there are *less than two contaminants in the two lower-mass bins*. Even though contamination is low, we choose not to neglect it as it affects the more crucial lower-mass bins. The contamination MF is subtracted from the completeness-corrected IMF computed in the previous section (Section 4.1).

We consider other potential sources of contamination. Nearby giants are very bright and thus are saturated in the *HST* images. Giants associated with the heavily extincted population described above are not simulated. However, as it can be seen in Fig. 2, they are redder than $J - H \sim 2$ mag and thus do not contaminate the PMS selection region. Evolved stars between the cluster and this redder population could, in principle, contaminate the PMS selection; they are, however, in negligible numbers due to the low stellar density

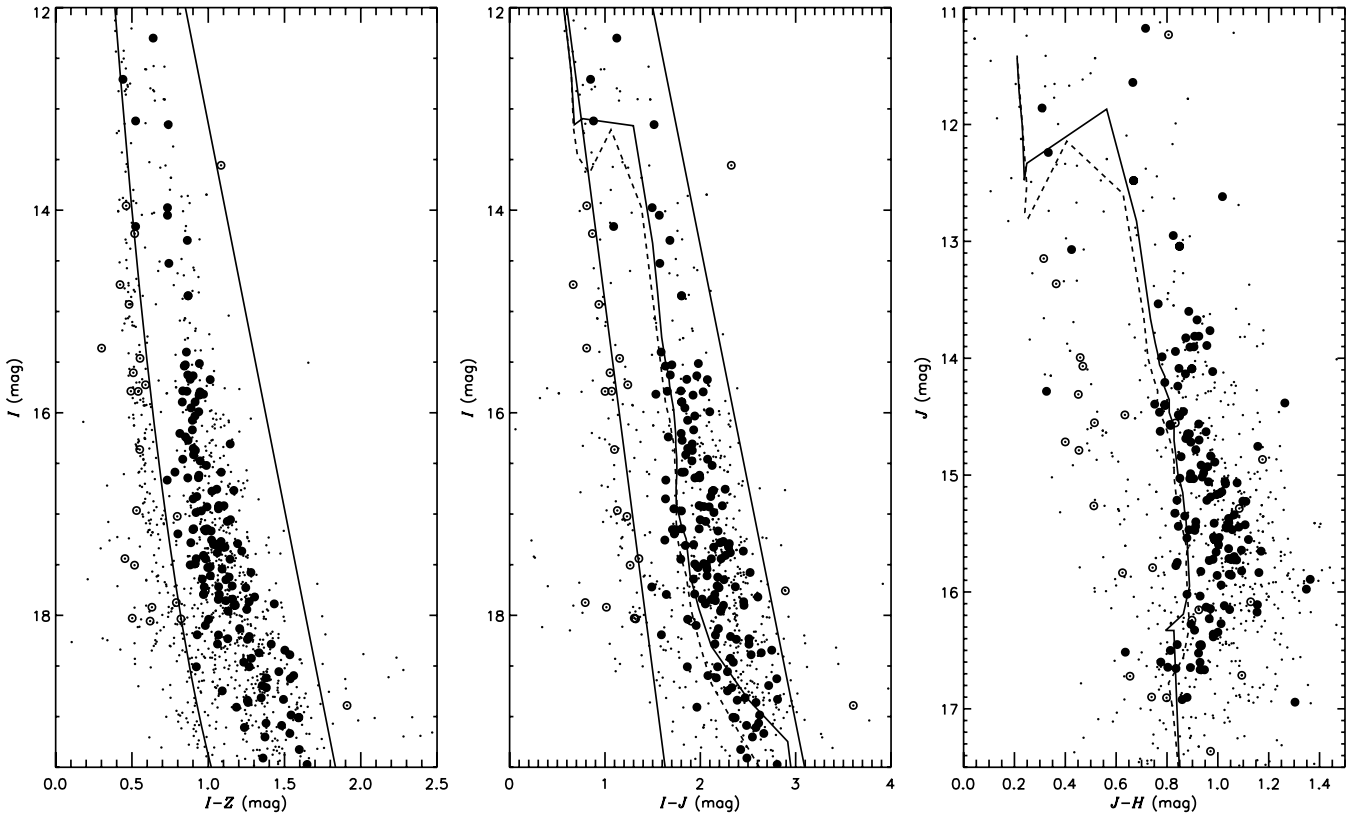

Figure 8. Colour–magnitude diagrams using the photometric catalogue from Oliveira et al. (2005). Small dots show the complete catalogue as described in that article and large circles represent the objects that fall on to the NICMOS mosaic (Fig. 1). The solid lines indicate the regions for selection of PMS candidates: filled circles show the PMS candidates. Solid and dashed lines are Siess et al. (2000) isochrones, respectively, for 2 and 3 Myr.

and the small volume sampled. The reddening screen behind the cluster further precludes giants nearer the Galactic centre as well as bright galaxies from being PMS contaminants, by making these extremely red and faint.

3.2 Higher- and solar-mass stars

We selected from the *IZJH* catalogue of Oliveira et al. (2005) a subset of stars from the same area in the sky as the NICMOS mosaic in Fig. 1. No attempt was made to convert photometry from different filter systems to merge the catalogues. This subset contains 176 objects from which we select PMS candidates based on colour–magnitude diagrams.

3.2.1 Identification of PMS stars and membership selection

As for the *HST* photometry, we follow the criteria based on I magnitude, $I - Z$ and $I - J$ colours to select PMS objects from the ground-based photometry (Fig. 8). $J - H$ does not play a role in the PMS selection here as there is negligible contamination from red stars in this magnitude range. The foreground field star sequence is scarcely populated in such a small area, indicating that contamination at brighter magnitudes is also very low. To increase the contrast of the field and PMS sequences, the diagrams also show the populations for the larger cluster area as described in Oliveira et al. (2005). Based on the criteria described above, 150 stars are identified as PMS candidates in the area covered by the NICMOS mosaic (Table 2).

Table 2. NGC 6611 higher-mass cluster candidates selected from the photometric catalogue of Oliveira et al. (2005). Positions are in the *2MASS* system. Columns provide the magnitudes and errors for I, Z, J, H, K and L'. $E(B - V) = 0.70$ mag is the extinction assumed for all PMS candidates. $M_{2\,\mathrm{Myr}}$ and $M_{3\,\mathrm{Myr}}$ are the masses of PMS objects, assuming an age of either 2 or 3 Myr. (Please see the Supporting Information section for details of the full table).

RA ($^{h\,m\,s}$)	Dec. ($^{d\,m\,s}$)	I (mag)	$I - Z$ (mag)	J (mag)	H (mag)	K (mag)	L' (mag)	$M_{2\,\mathrm{Myr}}$ ($\mathrm{M}_\odot$)	$M_{3\,\mathrm{Myr}}$ ($\mathrm{M}_\odot$)
18:18:40.09	−13:47:00.8	12.301 ± 0.006	0.639 ± 0.008	11.177 ± 0.003	10.462 ± 0.002	9.695 ± 0.004	8.317 ± 0.004	6.076	6.015
18:18:40.61	−13:47:44.4	12.708 ± 0.006	0.441 ± 0.008	11.859 ± 0.008	11.551 ± 0.002	11.335 ± 0.005	11.331 ± 0.008	4.914	4.902
18:18:42.25	−13:47:30.4	13.119 ± 0.006	0.524 ± 0.008	12.239 ± 0.007	11.906 ± 0.002	11.641 ± 0.004	11.531 ± 0.009	4.076	4.126
18:18:39.37	−13:47:11.8	13.975 ± 0.006	0.733 ± 0.008	12.480 ± 0.004	11.812 ± 0.003	11.551 ± 0.004	11.361 ± 0.008	2.791	2.500
18:18:39.83	−13:47:44.2	14.298 ± 0.006	0.863 ± 0.009	12.617 ± 0.011	11.599 ± 0.004	10.737 ± 0.008	9.637 ± 0.007	2.707	2.420
18:18:42.18	−13:47:22.4	14.845 ± 0.007	0.868 ± 0.009	13.042 ± 0.006	12.193 ± 0.002	11.832 ± 0.005	11.593 ± 0.009	2.474	2.285
				...					

3.2.2 *Reddening determination of PMS stars*

No single set of isochrones covers the complete mass range covered by our *HST* and ground-based catalogues. For the magnitude range covered in the Oliveira et al. (2005) catalogue, the most appropriate set of isochrones is that of Siess, Dufour & Forestini (2000) for solar metallicity that covers the mass range 0.1–7 $M_{\odot}$. This isochrone grid provides magnitudes calibrated according to the conversion table from Kenyon & Hartmann (1995). Those magnitudes are converted to the appropriate photometric system using published transformations: isochronal IR magnitudes were first converted to the 2MASS photometric system (Carpenter 2001) and then to the MKO system (Tokunaga et al. 2002); *I*-band magnitudes need no conversion.

We could have used the Siess isochrones and the *IJH* colour–magnitude diagram to determine the extinction towards the PMS candidates (theoretical *Z* magnitudes are not available), similar to what was described in Section 3.1.2 for the *HST* catalogue. However, and as expected for a brighter sample dominated by earlier type stars, the range of colours exhibited by these stars means that a large fraction of objects have a double reddening solution (see Section 3.1.2). In this regime, even small photometric errors can cause large uncertainties in $E(B-V)$. Furthermore, we think there are unquantified systematic effects in the isochronal *J* and *H* magnitudes due to successive photometric transformation. Taking all these factors into account, we consider this method to derive reddening rather unreliable *for this particular sample* and therefore chose to adopt a constant reddening $E(B-V)=0.7$ mag (see Section 3.1.2). Using this extinction value, intrinsic magnitudes are computed. Assuming an age of either 2 or 3 Myr and a distance of 1.8 kpc, we compute a stellar mass for each object using their intrinsic *I*-band magnitudes and the Siess et al. (2000) isochrones (Table 2).[5]

3.2.3 *Completeness correction and field star contamination*

Due to severe crowding towards the cluster centre and the relatively large number of saturated stars in the images, the ground-based data of this region are incomplete. To compute the completeness correction for the ground-based *I*-band catalogue, we make use of the much deeper *HST J* and *H* catalogues. The *I*-band *HST* catalogue cannot be used in this way because it saturates at $I\sim 16$ mag, corresponding (very approximately) to $I\sim 15.7$ mag in the ground-based catalogue. The procedure is rather simple. We start by assuming that the *HST J* and *H* catalogues are essentially complete. This is a reasonable assumption over most of the magnitude range of interest here, as incompleteness in the *IZJH HST* catalogue is driven by the *I* and *Z* bands. The *J*-band *HST* catalogue saturates, however, at about $J\sim 14$ mag (very approximately $J\sim 13.5$ mag ground based), thus we are unable to study completeness at the very bright end. We use objects detected in both *J* and *H* and look for their *positional counterparts* in the ground-based *IZJH* catalogue. This allows us to compute the recovery rate as a function of *HST J*-band magnitude. We need, however, an *I*-band completeness function. Using an empirical linear approximation, *HST J*-band magnitudes can be converted to MKO *J*-band magnitudes. Assuming a PMS age (Siess isochrone), the *J*-band magnitudes correspond uniquely to a ground-based *I*-band magnitude. The resulting *I*-band completeness function for the ground-based catalogue has a similar shape to the *HST I*-band completeness function shown in Fig. 6 but shifted to brighter magnitudes: it has a value just below unity to about $I\sim 15$ mag, falling after that as a second-degree polynomial to a value of about 0.1 at $I\sim 19$ mag. To construct the IMF, each PMS candidate is ascribed a weight equal to the inverse of the completeness correction at its observed *I*-band magnitude.

Field star contamination in the magnitude range of interest here is very small. Oliveira et al. (2005) used *IZ* photometry of an offset field to estimate foreground contamination. Following the same procedure, we estimate that nearly two objects might be field star contaminants in the NICMOS mosaic area in this magnitude range; this is an upper limit as we use only *IZ* criteria (no offset *JH* photometry is available). Such low level of contamination is consistent with what we found for the *HST* catalogue (Section 3.1.4). We chose not to apply any contamination correction to this data set, as we have no constraints on the likely masses of possible contaminants.

4 THE INITIAL MASS FUNCTION OF NGC 6611

4.1 Constructing the cluster IMF

In the previous section, we identified PMS candidates in NGC 6611 and computed their intrinsic *I*-band magnitudes. Using isochrones from Baraffe et al. (1998) and Siess et al. (2000) (respectively for the *HST* and ground-based data sets), we computed masses assuming a distance of 1.8 kpc and using either 2 or 3 Myr isochrones (Tables 1 and 2). We also estimate the contributions from completeness and contamination. Fig. 9 illustrates the corrections that are applied to the observed IMF to account for these two effects (in this particular case for the 2 Myr set of calculations). First, histograms are

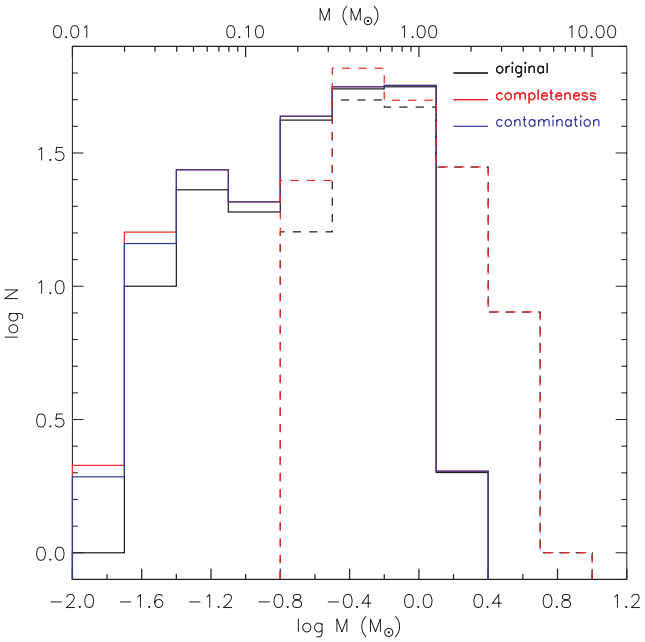

Figure 9. Completeness and contamination corrections to be applied to the computed IMFs, for the *HST* (solid line) and ground-based (dashed line) catalogues. The histograms show MFs (in black), corrected for incompleteness (red) and contamination (blue) for the *HST* catalogue only (see text). Contamination is small throughout, even in the brown dwarf mass bins. These histograms refer to the 2 Myr calculations, similar ones were constructed using 3 Myr isochrones.

[5] Oliveira et al. (2005) adopted a distance of 2 kpc, $A_V=3.4$ mag [$E(B-V)=0.9$ mag] and an age of 3 Myr. These values are different from those adopted here so estimated masses will differ.

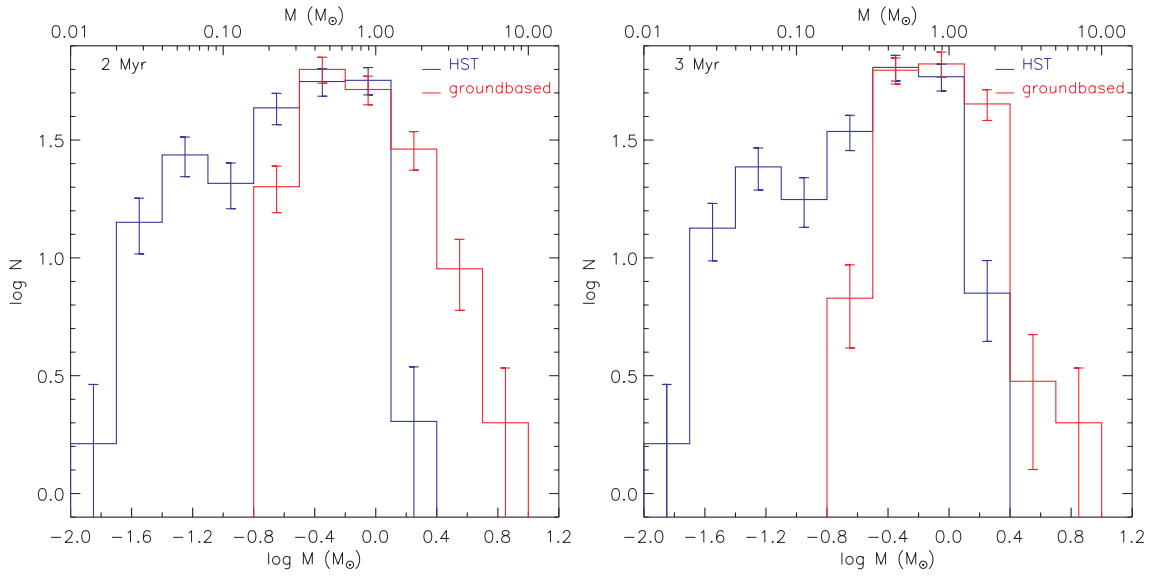

Figure 10. IMFs derived assuming an isochronal ages of 2 Myr (left-hand panel) and 3 Myr (right-hand panel). IMFs were constructed independently using the *HST* (blue) and ground-based (red) catalogues. The extreme bins in each histogram should be disregarded because they are not completely sampled by the catalogues. The two contributions agree remarkably well. The choice of isochrones also does not seem to influence the derived IMF in any significant way.

constructed for the PMS masses (bins of 0.3 dex in log mass): with unity weights (black histograms) and with weights equal to the inverse of the completeness function (red histograms) to perform the completeness correction. As described in Section 3.1.4, a contamination mass histogram is computed and is then subtracted from the completeness-corrected histogram (blue line). The contamination level is low throughout; in the two lower-mass bins there are, respectively, ∼0.2 and ∼1.2–1.5 contaminants (less than 10 per cent contamination). The final histograms (i.e. with completeness and contamination corrections applied) are the IMFs to be discussed in the following paragraphs. We apply *no correction to account for unresolved binaries*. The bin size of 0.3 dex was chosen to match other published IMFs (Section 4.3); however we tested that this choice does not significantly change the measured properties of the IMF. The extreme bins in each histogram should be ignored because the catalogues do not fully sample the mass range in those bins.

The ground-based and *HST* samples overlap in the mass range 0.15–1.5 $M_\odot$. The resulting IMFs are shown in Fig. 10 ($\log N$ versus $\log M/M_\odot$), assuming an age of 2 or 3 Myr. There is a very good agreement between the derived IMFs, for the bins where they overlap, despite different data sets and photometric systems, reddening treatments, theoretical models, etc. For these two mass bins, we average the two contributions to obtain the final IMFs.

Fig. 10 also shows that the choice of isochronal age does not make a significant difference in the constructed IMF properties. The most notable difference is the somewhat sharper fall towards higher masses for the 3 Myr determination. However, the two histograms are consistent within the statistical errors and furthermore these higher-mass bins are affected by low-number statistics and sampling effects. As the two IMFs are indistinguishable, we settle on the 2 Myr representation for further analysis and only when relevant provide comments using the 3-Myr-derived IMF.

We find that the IMF in NGC 6611 rises Salpeter like at higher masses, consistent with many determinations available in the literature (e.g. Dufton et al. 2006). The IMF flattens out between ∼1.25 and 0.3 $M_\odot$ (with the most likely peak position between 0.3 and 0.6 $M_\odot$) and then drops into the brown dwarf regime. There is an apparent secondary peak at ∼0.05 $M_\odot$. However, as we disregard the lower-mass bin, there is no evidence for a steep decline in the IMF towards lower masses.

We identified 30–35 brown dwarfs (respectively assuming 3 or 2 Myr) in our *observed sample* (before any completeness correction was applied; see Table 1). The brown dwarf to star ratio, defined as the ratio of the number of stars with masses in the ranges 0.02–0.08 $M_\odot$ and 0.08–10. $M_\odot$ (Briceño et al. 2002), is 0.19 ± 0.03 (0.17 ± 0.03 for 3 Myr). The star to brown dwarf ratio, defined by Andersen et al. (2008) as the ratio of the number of stars with masses in the ranges 0.08–1. $M_\odot$ and 0.03–0.08 $M_\odot$, is $4.4^{+0.9}_{-0.6}$ ($5.3^{+1.2}_{-0.8}$ for 3 Myr). In the next sections, we will compare these observed properties both with theoretical IMF representations and with other young clusters.

4.2 Comparison with IMF theoretical expectations

The most commonly used theoretical representations of the field IMF make use of a multiple-part power law (e.g. Kroupa 2001) or a Scalo-like lognormal function (e.g. Chabrier 2005). Both functional forms describe the IMF as reaching a peak at a few tenths of a solar mass and falling both into the higher-mass and into brown dwarf regimes. The Kroupa (2001) power-law IMF (in linear units) is characterized by the index α and is defined as $\psi(M) = \mathrm{d}N/\mathrm{d}M \propto M^{-\alpha_i}$. The average Galactic-field IMF (uncorrected for unresolved binaries) is Salpeter like to 0.5 $M_\odot$ with $\alpha_1 \sim +2.3$ – in this representation, the Salpeter slope is equal to +2.35; between 0.08 and 0.5 $M_\odot$, the IMF flattens somewhat, continuing to rise but less steeply with $\alpha_2 \sim +1.3$; the IMF drops into the brown dwarf regime with $\alpha_3 \sim +0.3$ (Kroupa 2001). The lognormal description (in logarithmic units) has the form $\xi = \mathrm{d}N/\mathrm{d}\log M \propto \exp[-(\log m - \log m_\mathrm{c})^2/2\sigma^2]$. Chabrier (2005) find that $m_\mathrm{c} = 0.25\,M_\odot$ and $\sigma = 0.55$ are required to reproduce the stellar MF in the solar neighbourhood (no correction for unresolved binaries). This lognormal distribution is also found to fit well the MFs of a number of open clusters like Blanco 1 (Moraux et al. 2007) and the Pleiades (Moraux et al. 2003).

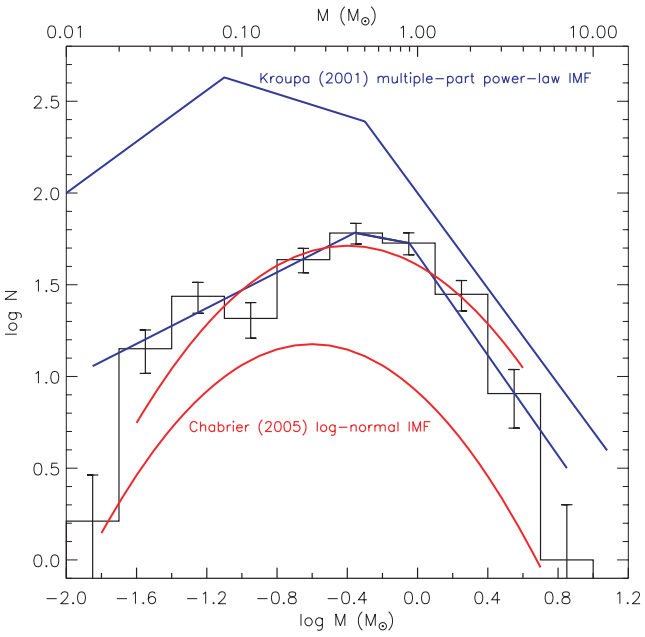

Figure 11. Comparison of the IMF of NGC 6611 with well-known theoretical functional forms: the multiple-part power-law IMF (labelled blue line; Kroupa 2001) and the lognormal IMF (labelled red line; Chabrier 2005). We have fitted such functions to the observed IMF (ignoring the two extreme bins); the most adequate fits are overplotted on the IMF. Both when compared to the power-law and lognormal formulations, the NGC 6611 IMF peaks at a slightly higher mass, $\sim$0.45 $M_\odot$ (see text).

In Fig. 11, we compare the IMF of NGC 6611 with both the power-law and lognormal IMFs. We stress that we have applied no correction to account for unresolved binary systems. In terms of a power-law representation, we find that the best fits are provided by power-law indices α_i of +2.36, +1.18 and +0.52, respectively, for masses $\gtrsim$0.9 $M_\odot$, between $\sim$0.9 and $\sim$0.45 $M_\odot$ and $\lesssim$0.45 $M_\odot$. These indices are consistent with those determined by Kroupa (2001) within the uncertainties. However, the IMF in NGC 6611 flattens at higher masses ($\sim$0.9 $M_\odot$ instead of 0.5 $M_\odot$) and starts to fall sharply also at higher masses ($\sim$0.45 $M_\odot$ instead of 0.1 $M_\odot$). When using the lognormal function, we determine $m_c \sim 0.40 \pm 0.04\,M_\odot$ and $\sigma = 0.56 \pm 0.04$. While the width of the distributions is similar in NGC 6611 and in the field, the peak occurs at higher masses in NGC 6611. Both the comparison with the power law and lognormal IMFs suggests that the IMF in NGC 6611 peaks at higher mass.

4.3 Comparison with other young clusters

In this section, we compare the IMF of NGC 6611 with those of other young clusters and associations compiled from the literature: Taurus (Luhman 2004), the ONC (Muench et al. 2002; Slesnick et al. 2004), IC 348 (Luhman et al. 2003), Chamaeleon I (Luhman 2007) and NGC 2024 (Levine et al. 2006). Slesnick et al. (2004) constructed the IMF for the ONC using the D'Antona & Mazzitelli (1997) evolutionary tracks; for the remaining determinations, the Baraffe et al. (1998) models were used. These clusters are younger than a few Myr in order to minimize effects like dynamical evolution and mass segregation. No correction for binarity was applied to the IMFs of *any* of the clusters discussed here, assuring that these IMFs are comparable, so long as their binary properties are not too different.[6]

In Fig. 12, we show the IMFs of the clusters considered here. A notable difference is that the IMFs of both Taurus and NGC 6611 (Fig. 12, left-hand panel) seem to peak at slightly higher masses than those of the other young clusters (Fig. 12, right-hand panel): the IMF peaks are at $\sim$0.8 $M_\odot$ and $\sim$0.5 $M_\odot$, respectively, for Taurus and NGC 6611 and at 0.1–0.2 $M_\odot$ for the other clusters. Another quantity also used to characterize the IMF – and that might be less dependent on the adopted binning – is the characteristic mass, defined as the mid-point of the IMF plateau (Elmegreen, Klessen & Wilson 2008); for most clusters in Fig. 12, it occurs at $\sim$0.3 $M_\odot$ while for NGC 6611 it is at $\sim$0.45 $M_\odot$.

We perform a Kolmogorov–Smirnov statistical comparison to test whether the observed IMF differences are significant. When the IMF of NGC 6611 is compared to those of Taurus and the ONC, the probability that they are drawn for the same cumulative distribution is 0.1 and 4×10^{-6}, respectively. The probability that the IMFs of the ONC and IC 348 are drawn from the same distribution is 0.65, confirming that indeed they are very similar. This analysis confirms that the shape of the IMF of NGC 6611 resembles more that of Taurus, and it is very unlikely to mirror that of the ONC.

We can also compare the relative numbers of stars and brown dwarfs for these clusters. We should point out that such ratios are problematic to compute as it is difficult to achieve survey completeness: for instance, Taurus is a very spatially extended region and Cambrésy et al. (2006) claim that current IC 348 surveys are still incomplete. We list available ratios for the six clusters in Table 3. The brown dwarf to star ratio varies from 0.13 for IC 348 to 0.30 for the ONC and NGC 2024. The brown dwarf to star ratios of the ONC, NGC 2024 and Chamaeleon I are similar within the uncertainties while those for Taurus and IC 348 are lower. The ratio we determine for NGC 6611 is consistent with that of Taurus. The ratio of stars to brown dwarfs (as defined by Andersen et al. 2008) varies from $3.3^{+0.8}_{-0.7}$ for the ONC to $8.3^{+3.3}_{-2.6}$ for IC 348. The ratio for NGC 6611 is between those for Chamaeleon I and Taurus.

An issue still being debated is whether the shape of the IMF shows any imprint of the conditions under which the star formation process takes place. Those initial conditions are impossible to constrain directly, but we can try to infer them from the observed present-day properties of the resulting stellar populations. We use cluster data available in the literature (Andersen et al. 2008, and references therein) to crudely estimate an average stellar surface density of PMS stars (dividing the number of stars with masses in the range 0.03–1 $M_\odot$ by the area) for each cluster. We also estimate the average ionizing flux at the position of the PMS stars for NGC 6611 and the ONC – using tabulated total ionizing fluxes from Osterbrock & Ferland (2006); the other populations contain no O-stars. These and other relevant cluster properties are listed in Table 3.

The ONC is the most extreme of these associations in terms of present-day stellar density. Chamaeleon I, NGC 2024 and IC 348 all have similar stellar densities and are less dense than NGC 6611 and the ONC. Taurus, on the other hand, is the prototypical example of a low-density quiescent star-forming environment. The average ionizing fluxes for NGC 6611 and the ONC are similar, despite the fact that NGC 6611 has more and more powerful ionizing sources.

[6] Chabrier (2005) has shown that when unresolved binaries are taken into account, the peak of the disc IMF moves to slightly lower masses (from 0.25 to 0.20 $M_\odot$).

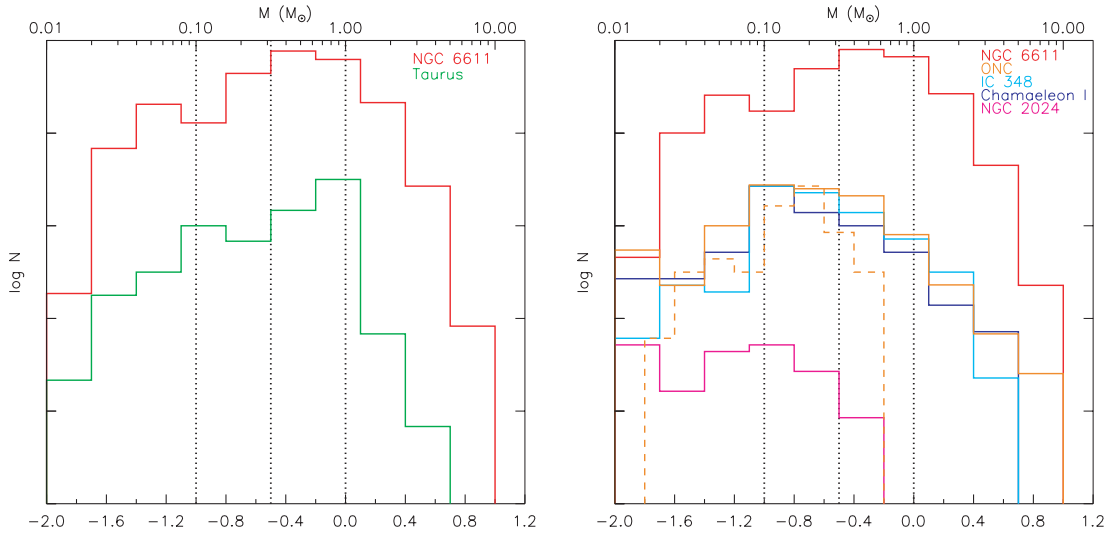

Figure 12. Comparison between IMFs for several young clusters and associations: NGC 6611 (this work, red), Taurus (Luhman 2004, green), the ONC (Muench et al. 2002, orange solid line, rebinned to match other clusters; Slesnick et al. 2004, orange dashed line), IC 348 (Luhman et al. 2003, cyan), Chamaeleon I (Luhman 2007, blue) and NGC 2024 (Levine et al. 2006, magenta). The *y*-axis is in arbitrary log *N* units and published cluster IMFs have been renormalized for display purposes. The vertical dotted lines indicate the typical positions of the plateau and the characteristic mass M_c for most clusters. The peaks of the IMFs of Taurus and NGC 6611 seem to occur at higher masses.

Table 3. Compiled cluster and IMF properties (relevant to the comparison described in Section 4.3). References for the ratios (see text for definitions) are as follows: 1, this work; 2, Luhman (2000); 3, Andersen et al. (2008); 4, Levine et al. (2006); 5, Luhman (2007); 6, Luhman et al. (2003); 7, Luhman (2004) and 8, Guieu et al. (2006). The other cluster properties are compiled from Andersen et al. (2008, and references therein), Luhman (2008), Herbst (2008), Meyer et al. (2008), Muench et al. (2008), Oliveira (2008) and Kenyon, Goméz & Whitney (2008).

Cluster	Age (Myr)	Distance (pc)	Peak ($M_\odot$)	Brown dwarf/star ratio	Ref	Star/brown dwarf ratio	Ref	Density (star pc^{-2})	Massive member	⟨Ionizing flux⟩ (photon s^{-1} pc^{-2})
NGC 6611	2−3	1 800	0.5	0.19 ± 0.03†	1	$4.4^{+0.9}_{-0.6}$†	1	138	O3−O5	1.8×10^{49}
ONC	1	480	0.1	0.26 ± 0.04	2	$3.3^{+0.8}_{-0.7}$	3	365	O7	1.0×10^{49}
				0.30 ± 0.05	4					
Cham I	2	160	0.1	0.26 ± 0.06	5	$4.0^{+3.7}_{-2.1}$	3	60	B6	
NGC 2024	1	460	0.1	0.30 ± 0.05	4	$3.8^{+2.1}_{-1.5}$	3	80	Early B	
IC 348	2	315	0.1	0.12 ± 0.03	6	$8.3^{+3.3}_{-2.6}$	3	90	B5	
Taurus	1−3	140	0.8	0.18 ± 0.04	7	$6.0^{+2.6}_{-2.0}$	3	5	A6	
				0.23 ± 0.05	8					

†Ratios assuming a cluster age of 2 Myr (see text).

NGC 6611 is the most massive of the clusters considered here (Bonatto et al. 2006).

The IMFs of the ONC, Chamaeleon I and IC 348 are similar, despite their different stellar densities; although compared to these other clusters IC 348 has an abnormally low number of brown dwarfs. The IMF of NGC 6611 most resembles that of Taurus, in terms of both peak mass and relative number of brown dwarfs, but the star formation environments of NGC 6611 and Taurus are dramatically different. The IMFs of NGC 6611 and the ONC are very different, despite both being examples of low-mass star formation accompanied by O- and B-type stars.

The properties described in Table 3 are *present-day cluster properties*, and the ages of the clusters span 1–3 Myr. Some dynamical evolution has probably occurred so the populations were likely denser and, in the cases of NGC 6611 and the ONC, the PMS stars were likely nearer to the ionizing sources. We only analyse a small central region of NGC 6611, and it is not possible to assess at the moment whether the IMF we constructed is representative of the whole cluster. Still, no clear trend has emerged so far that relates IMF observed properties with known cluster properties like ionizing radiation or stellar density. Our results suggest that the radiation field from the O-stars does not play a dominant role in shaping the lower-mass IMF.

4.4 Discussion and implications

The goal of this paper was to investigate the properties of the low-mass IMF of NGC 6611, and in particular the brown dwarf frequency and peak or characteristic mass. The intrinsic complexity of the IMF and the still limited understanding of which processes are dominant in shaping it (Bonnell et al. 2007; Elmegreen 2008) means that it is not possible to model an individual IMF (except by using analytic parametrizations like the ones described in Section 4.2). Instead, by comparing the IMFs of clusters and

associations with different present-day properties, we can try to constrain which physical conditions and eventually which physical process are more important.

As recently reviewed by Elmegreen (2008), there are three main types of star formation theory: fragmentation (both gravitational and turbulent), competitive accretion and interruption (that includes both ejection and photoevaporation scenarios). These theories need to be able to explain not only the properties of the IMF, but also the binary and circumstellar disc fractions across all masses and the dynamical properties of stellar populations.

There is abundant observational evidence that supports a similar formation mechanism for brown dwarfs and solar-mass stars (Luhman et al. 2006). However, an open question in the understanding of brown dwarf (and low-mass star) formation is how the low-mass cores are stopped from accreting further so that their final mass can remain sub-stellar. Two mechanisms have been proposed to halt accretion: ejection of newly formed fragments and photoevaporation of collapsing cores. The ejection scenario (e.g. Reipurth & Clarke 2001) proposes that the smallest clumps in multiple systems are ejected and are thus denied access to the molecular gas reservoir. There are several problems with this scenario, namely that the spatial distribution of solar-mass stars and brown dwarfs in clusters seems to be similar (Luhman 2004; Luhman et al. 2006), and that both the binary (Burgasser et al. 2007) and disc properties (Jayawardhana et al. 2003) of the two populations are also similar. The photoevaporation scenario (Whitworth & Zinnecker 2004) relies on the proximity to massive O-stars to stop accretion. This would imply that we should find a higher brown dwarf to star ratio in OB associations than in quieter regions; this is not supported by our observations in NGC 6611.

Recently, Bonnell, Clark & Bate (2008) suggested that gravitational fragmentation of infalling gas into stellar clusters can form low-mass stars and brown dwarfs without invoking any additional mechanism. Increased gas density within the collapse region gives rise to a filamentary-like structure within which the Jeans mass is lower, allowing lower-mass clumps to form; the infall velocity of the gas prevents the low-mass clump from accreting significant amounts of gas, preserving its low-mass or brown dwarf status. Another mechanism like turbulent fragmentation would, however, be necessary to form brown dwarfs in low-density regions (Bonnell et al. 2008). As discussed in the previous section, the observations do not suggest any variation of brown dwarf fraction with *present-day* average stellar density.

The fact that massive star feedback does not seem to have a significant impact on *low-mass star formation* is not necessarily surprising. The idea that competitive accretion in a cluster environment is an important process in the formation of the more massive stars is gaining favour (Bonnell & Bate 2006; Bonnell et al. 2007; Elmegreen 2008). In this context, fragmentation produces lower-mass stars and a few higher-mass stars form subsequently by accreting more mass in the cluster gravitational potential. This would imply that by the time the most massive stars are formed, the main properties of the IMF are already defined (Bonnell & Bate 2006; Bonnell et al. 2007); we would then not expect *significant* differences between the IMFs of OB associations and quiet star-forming regions, consistent with what was shown in Section 4.3.

The shape of the IMF between 0.1 and 1 $M_\odot$ also presents a challenge. The characteristic mass of the IMF M_c is observed to be essentially constant for most star-forming regions (see review by Elmegreen et al. 2008). Based on numerical simulations, it has been proposed that this characteristic mass (and the associated plateau) is related to the thermal Jeans mass at the onset of (isothermal) collapse (e.g. Bate & Bonnell 2005). One could then intuitively expect the plateau properties to vary with the environmental conditions, via, for instance, the dependence of the Jeans mass on the density in the molecular core. However, Elmegreen et al. (2008) show that, if grain–gas coupling is taken into account, the thermal Jeans mass depends only weakly on environmental factors like density, temperature, metallicity and radiation field. Indeed, recent simulations by Bonnell, Clarke & Bate (2006), using a more realistic equation of state to allow for the coupling of the gas and dust at the high densities typical of star-forming regions, predict a characteristic mass that is relatively independent of the initial conditions for star formation.

Fig. 12 shows some significant differences in the observed IMFs of young clusters. At present, and in the absence of any trend of IMF properties with cluster properties, we remain unable to explain such differences. It is possible that the lower-mass IMF is shaped by a combination of different processes and that a particular effect might become dominant depending on the environmental conditions.

5 SUMMARY

We present results based on the deepest images to date in the central region of NGC 6611. The observations were obtained with ACS/WFC and NICMOS on board *HST* and reach down to $I \sim 26$ mag. We use this photometric catalogue to construct the cluster IMF from 1.5 to 0.02 $M_\odot$. We use the photometric catalogue from Oliveira et al. (2005) to extend this IMF to higher masses ($\sim$7 $M_\odot$).

We find that the IMF of NGC 6611 is well described by a lognormal distribution. However, both when compared to the Kroupa (2001) multiple power law and Chabrier (2005) lognormal distributions, the IMF of NGC 6611 seems to peak at higher masses than the Galactic field and the solar neighbourhood IMF. The higher-mass slope is Salpeter like, and we find no evidence of a sharp decline towards the brown dwarf regime. We identified 30–35 brown dwarf candidates, depending on the assumed cluster age.

We compare the IMF we derive for NGC 6611 to those of other clusters available in the literature. We find conclusive evidence that the IMF of NGC 6611 more closely resembles that of Taurus than that of the ONC. This is surprising since Taurus is the prototypical low-density star-forming region while both NGC 6611 and the ONC are examples of low-mass star formation in OB associations. Even though the present-day properties of these two clusters (stellar density and ionizing radiation field) are similar, a KS test shows that their observed IMFs are not drawn from the same mass distribution. Our analysis yields no trend that relates either present-day stellar density or intensity of the ionization field with observed IMF properties. Still, the fact that the IMFs of Taurus and NGC 6611 are similar suggests that the formation of lower-mass stars can be unaffected by their massive siblings.

Even though there is mounting evidence that suggests variations in the lower-mass IMF for young clusters, we are still at present unable to fully explain them. A large sample of clusters, observed and analysed consistently, is necessary to try to investigate environmental links in any detail. New instrumentation is already allowing us to investigate the lower-mass IMFs in extragalactic environments. In that context, IMFs constructed solely on the basis of photometric catalogues will become increasingly important, as they offer the only reliable comparisons with extragalactic determinations.

ACKNOWLEDGMENTS

The authors would like to thank the STScI helpdesk for invaluable support in preparing and reducing the observations. STSDAS and

PYRAF are products of the Space Telescope Science Institute, which is operated by AURA for NASA. The authors also acknowledge the support of the UKIRT and INT staff. JMO acknowledges the support of the UK Science and Technology Facilities Council (STFC). We thank the referee Barbara Whitney for her comments.

REFERENCES

Andersen M., Meyer M. R., Greissl J., Aversa A., 2008, ApJ, 683, 183
Baraffe I., Chabrier G., Allard F., Hauschildt P. H., 1998, A&A, 337, 403
Barker E. et al., 2007, NICMOS Instrument Handbook. Version 10.0. Space Telescope Science Institute, Baltimore
Bate M. R., Bonnell I. A., 2005, MNRAS, 356, 1201
Belikov A. N., Kharchenko N. V., Piskunov A. E., Schilbach E., 1999, A&AS, 134, 525
Belikov A. N., Kharchenko N. V., Piskunov A. E., Schilbach E., 2000, A&A, 358, 886
Bessell M. S., Brett J. M., 1988, PASP, 100, 1134
Boffi F. R. et al., 2007, ACS Instrument Handbook. Version 8.0. Space Telescope Science Institute, Baltimore
Bonatto C., Santos J. F. C. Jr, Bica E., 2006, A&A, 445, 567,
Bonnell I. A., Bate M. R., 2006, MNRAS, 370, 488
Bonnell I. A., Clarke C. J., Bate M. R., 2006, MNRAS, 368, 1296
Bonnell I. A., Clark P., Bate M. R., 2008, MNRAS, 389, 1556
Bonnell I. A., Larson R. B., Zinnecker H., 2007, in Reipurth B., Jewitt D., Keil K., eds, Protostars and Planets V. University of Arizona Press, Tucson, p. 149
Briceño C., Luhman K. L., Hartmann L., Stauffer J. R., Kirkpatrick J. D., 2002, ApJ, 580, 317
Burgasser A. J., Reid I. N., Siegler N., Close L., Allen P., Lowrance P., Gizis J., 2007, in Reipurth B., Jewitt D., Keil K., eds, Protostars and Planets V. University of Arizona Press, Tucson, p. 427
Cambrésy L., Petropoulou V., Kontizas M., Kontizas E., 2006, A&A, 445, 999
Cardelli J. A., Clayton G. C., Mathis J. S., 1989, ApJ, 345, 245
Carpenter J. M., 2001, AJ, 121, 2851
Chabrier G., 2005, in Corbelli E., Palla F., Zinnecker H., eds, Astrophysics and Space Science Library. The Initial Mass Function 50 years later, Vol. 327. Springer, Dordrecht, p. 41
Chen B. et al., 2001, ApJ, 553, 184
Chiu K., Fan X., Leggett S. K., Golimowski D. A., Zheng W., Geballe T. R., Schneider D. P., Brinkmann J., 2006, AJ, 131, 2722
D'Antona F., Mazzitelli I., 1997, Mem. Soc. Astron. Italiana, 68, 807
Davis L. E., 1994, A reference guide to the IRAF/DAOPHOT Package
de Jong R. S., 2006, Instrument Science Report NICMOS 2006-003
Dufton P. L. et al., 2006, A&A, 457, 265
Elmegreen B. G., 2008, The Evolving ISM in the Milky Way and Nearby Galaxies: Recycling in the Nearby Universe. 4th Spitzer Science Center Conference, preprint (arXiv:0803.3154)
Elmegreen B. G., Klessen R. S., Wilson C. D., 2008, ApJ, 681, 365
Gray D. F., 1992, The Observation and Analysis of Stellar Photospheres. Cambridge Univ. Press, Cambridge
Guarcello M. G., Prisinzano L., Micela G., Damiani F., Peres G., Sciortino S., 2007, A&A, 462, 245
Guieu S., Dougados C., Monin J.-L., Magnier E., Martin E. L., 2006, A&A, 446, 485
Herbst W., 2008, in Reipurth B., ed., ASP Conf. Ser., Handbook of Star Forming Regions. Astron. Soc. Pac., San Francisco, in press
Hillenbrand L. A., Massey P., Strom S. E., Merrill K. M., 1993, AJ, 106, 1906
Indebetouw R., Robitaille T. P., Whitney B. A., Churchwell E., Babler B., Meade M., Watson C., Wolfire M., 2007, ApJ, 666, 321
Jayawardhana R., Ardila D. R., Stelzer B., Haisch K. E. Jr, 2003, AJ, 126, 1515
Jeffries R. D., Naylor T., Devey C. R., Totten E. J., 2004, MNRAS, 351, 1401
Kenyon S. J., Hartmann L., 1995, ApJS, 101, 117
Kenyon S. J., Goméz M., Whitney B. A., 2008, in Reipurth B., ed., ASP Con. Ser., Handbook of Star Forming Regions. Astron. Soc. Pac., San Francisco, in press
Knapp G. R. et al., 2004, AJ, 127, 3553
Kraus A. L., White R. J., Hillenbrand L. A., 2005, ApJ, 633, 452
Kraus A. L., White R. J., Hillenbrand L. A., 2006, ApJ, 649, 306
Krist J. E., Golimowski A. A., Schroeder A. J., Henry T. J., 1998, PASP, 110, 1046
Kroupa P., 2001, MNRAS, 322, 231
Laidler V. et al., 2005, SYNPHOT User's Guide. Version 5. Space Telescope Science Institute, Baltimore
Leggett S. K., 1992, ApJS, 82, 351
Leggett S. K., Allard F., Berriman G., Dahn C. C., Hauschildt P. H., 1996, ApJS, 104, 117
Leggett S. K., Allard F., Dahn C., Hauschildt P. H., Kerr T. H., Rayner J., 2000, ApJ, 535, 965
Levine J. L., Steinhauer A., Elston R. J., Lada E. A., 2006, ApJ, 646, 1215
Luhman K. L., 2000, ApJ, 544, 1044
Luhman K. L., 2004, ApJ, 617, 1216
Luhman K. L., 2007, ApJS, 173, 104
Luhman K. L., 2008, in Reipurth B., ed., ASP Conf. Ser., Handbook of Star Forming Regions. Astron. Soc. Pac., San Francisco, in press (arXiv:0808.3207)
Luhman K. L., Stauffer J. R., Muench A. A., Rieke G. H., Lada E. A., Bouvier J., Lada C. J., 2003, ApJ, 593, 1093
Luhman K. L., Joergens V., Lada C., Muzerolle J., Pascucci I., White R., 2006, in Reipurth B., Jewitt D., Keil K., eds, Protostars and Planets V. University of Arizona Press, Tucson, p. 443
Marigo P., Girardi L., Bressan A., Groenewegen M. A. T., Silva L., Granato G. L., 2008, A&A, 482, 883
Marshall D. J., Robin A. C., Reylé C., Schultheis M., Picaud S., 2006, A&A, 453, 635
Massey P., Johnson K. E., DeGioia-Eastwood K., 1995, ApJ, 454, 151
Meyer M. R., Levine J. L., Lada E. A., Bowler B. P., Kandori R., 2008, in Reipurth B., ed., ASP Conf. Ser., Handbook of Star Forming Regions. Astron. Soc. Pac., San Francisco, in press
Moraux E., Bouvier J., Stauffer J. R., Cuillandre J.-C., 2003, A&A, 400, 891
Moraux E., Bouvier J., Stauffer J. R., Barrado y Navascués D., Cuillandre J.-C., 2007, A&A, 471, 499
Muench A. A., Lada E. A., Lada C. J., Alves J., 2002, ApJ, 573, 366
Muench A., Getman K., Hillenbrand L., Preibish T., 2008, in Reipurth B., ed., ASP Conf. Ser., Handbook of Star Forming Regions. Astron. Soc. Pac, San Francisco, in press
Naylor T., Totten E. J., Jeffries R. D., Pozzo M., Devey C. R., Thompson S. A., 2002, MNRAS, 335, 291
Oliveira J. M., 2008, in Reipurth B., ed., ASP Con. Ser., Handbook of Star Forming Regions. Astron. Soc. Pac, San Francisco, in press (arXiv:0809.3735)
Oliveira J. M., Jeffries R. D., van Loon J. Th., 2004, MNRAS, 347, 1327
Oliveira J. M., Jeffries R. D., van Loon J. Th., Littlefair S. P., Naylor T., 2005, MNRAS, 358, L21
Osterbrock D. E., Ferland G. J., 2006, Astrophysics of Gaseous Nebulae and Active Galactic Nuclei, 2nd edn. University Science Books, Sausalito, California, p. 27
Pavlovsky C. et al., 2006, ACS Data Handbook, Version 5.0. Space Telescope Science Institute, Baltimore
Reid I. N., Hawley S. L., 2000, New Light on Dark Stars: Red Dwarfs, Low Mass Stars, Brown Dwarfs. Springer, New York [Springer-Praxis series in Astronomy & Astrophysics]
Reipurth B., Clarke C., 2001, AJ, 122, 432
Rejkuba M., Greggio L., Harris W. E., Harris G. L. H., Peng E. W., 2005, ApJ, 631, 262
Riess A., Mack J., 2004, Instrument Science Report ACS 2004-006. Space Telescope Science Institute, Baltimore
Robitaille T. P., Whitney B. A., Indebetouw R., Wood K., 2007, ApJS, 169, 328
Siess L., Dufour E., Forestini M., 2000, A&A, 358, 593

Sirianni M. et al., 2005, PASP, 117, 1049
Slesnick C. L., Hillenbrand L. A., Carpenter J. M., 2004, ApJ, 610, 1045
Stetson P. B., 1987, PASP, 99, 191
Stetson P. B., 1991, in Janes K. A. ed., ASP Conf. Ser. Vol. 13, The Formation and Evolution of Star Clusters. Astron Soc. Pac., San Francisco, p. 88
Tokunaga A. T., Simons D. A., Vacca W. D., 2002, PASP, 114, 180
Vallée J. P., 2008, AJ, 135, 1301
Whitworth A. P., Zinnecker H., 2004, A&A, 427, 299
Zheng Z., Flynn C., Gould A., Bahcall J. N., Salim S., 2004, ApJ, 610, 500

SUPPORTING INFORMATION

The following supporting information is available for this article.

Table 1. NGC 6611 cluster candidates selected from the *HST* photometric catalogue.

Table 2. NGC 6611 higher-mass cluster candidates selected from the photometric catalogue of Oliveira et al. (2005).

Supporting Information may be found in the online version of this article.

Please note: Wiley-Blackwell are not responsible for the content or functionality of any supporting information supplied by the authors. Any queries (other than missing material) should be directed to the corresponding author for the article.

This paper has been typeset from a TEX/LATEX file prepared by the author.